JGR Solid Earth

RESEARCH ARTICLE
10.1029/2019JB017442

Constraining Absolute Plate Motions Since the Triassic

Michael G. Tetley[1,2,3], Simon E. Williams[1], Michael Gurnis[2], Nicolas Flament[4], and R. Dietmar Müller[1]

[1]EarthByte Group, School of Geosciences, University of Sydney, Sydney, New South Wales, Australia, [2]Seismological Laboratory, California Institute of Technology, Pasadena, CA, USA, [3]Data61, CSIRO, Australian Technology Park, Eveleigh, New South Wales, Australia, [4]School of Earth and Environmental Sciences, University of Wollongong, Wollongong, New South Wales, Australia

Abstract The absolute motion of tectonic plates since Pangea can be derived from observations of hotspot trails, paleomagnetism, or seismic tomography. However, fitting observations is typically carried out in isolation without consideration for the fit to unused data or whether the resulting plate motions are geodynamically plausible. Through the joint evaluation of global hotspot track observations (for times <80 Ma), first-order estimates of net lithospheric rotation (NLR), and parameter estimation for paleo–trench migration (TM), we present a suite of geodynamically consistent, data-optimized global absolute reference frames from 220 Ma to the present. Each absolute plate motion (APM) model was evaluated against six published APM models, together incorporating the full range of primary data constraints. Model performance for published and new models was quantified through a standard statistical analyses using three key diagnostic global metrics: root-mean square plate velocities, NLR characteristics, and TM behavior. Additionally, models were assessed for consistency with published global paleomagnetic data and for ages <80 Ma for predicted relative hotspot motion, track geometry, and time dependence. Optimized APM models demonstrated significantly improved global fit with geological and geophysical observations while performing consistently with geodynamic constraints. Critically, APM models derived by limiting average rates of NLR to ~0.05°/Myr and absolute TM velocities to ~27-mm/year fit geological observations including hotspot tracks. This suggests that this range of NLR and TM estimates may be appropriate for Earth over the last 220 Myr, providing a key step toward the practical integration of numerical geodynamics into plate tectonic reconstructions.

Key Points:
- New global absolute plate motion models integrating geodynamic principles and geological observations for the last 220 million years
- Models derived by constraining trench migration and net lithospheric rotation produce optimum plate motion characteristics
- New models of absolute motion for nine hotspots from the Pacific, Indian, and Atlantic Oceans

Supporting Information:
- Supporting Information S1
- Table S1
- Table S2
- Table S3
- Data S1

Correspondence to:
M. G. Tetley,
michael.tetley@univ-lyon1.fr

Citation:
Tetley, M. G., Williams, S. E., Gurnis, M., Flament, N., & Müller, R. D. (2019). Constraining absolute plate motions since the Triassic. *Journal of Geophysical Research: Solid Earth*, *124*, 7231–7258. https://doi.org/10.1029/2019JB017442

Received 29 JAN 2019
Accepted 31 MAY 2019
Accepted article online 7 JUN 2019
Published online 6 JUL 2019

1. Introduction

The surface of the Earth consists of a continuous tessellation of rigid tectonic plates separated by deforming plate boundaries, together forming a regime of rigid motion. Individual plate motions, themselves an expression of Earth's dynamics on both local and global scales, can be accurately measured at present day with space geodesy (Argus & Heflin, 1995; DeMets et al., 2010; Gordon & Stein, 1992); however, for Earth's geological history these motions must be inferred from geophysical and geological observations. For the past ~200 Myr the primary data resource utilized for the creation of plate tectonic reconstructions is the analysis of the seafloor spreading record as preserved in the observable present-day oceanic crust (Hellinger, 1981; Müller et al., 2016; Seton et al., 2012). These observations provide detailed information to constrain the distribution and relative kinematic motions that exist between adjacent plates but do not contain the information necessary to constrain the absolute locations of these plates on the surface of the Earth relative to a fixed quantity such as the spin axis or long-lived mantle structures (Figure 1). To address this, relative plate motion (RPM) models are traditionally connected to a global tectonic reference frame, or absolute plate motion (APM) model, effectively linking the relative surface motions to a fixed reference point, providing the missing the piece of the puzzle (Müller et al., 2016, 2019). The development of APM models remains a significant challenge, as the selection of data constraints and model assumptions produce diverse APM behavior, directly affecting key tectonic characteristics of RPM models including spreading rates and directions, subduction zone kinematics, and magnitudes of global net lithospheric rotation (NLR), that is the differential motion of the lithosphere with respect to the underlying mantle (Becker, 2006; Torsvik, Müller, et al., 2008, Torsvik et al., 2010; Conrad & Behn, 2010; Becker et al., 2015; Williams et al., 2015, 2016). A requirement of any APM model is the identification of a reliable reference data source that is independent of any observed RPM relationships and ideally remains

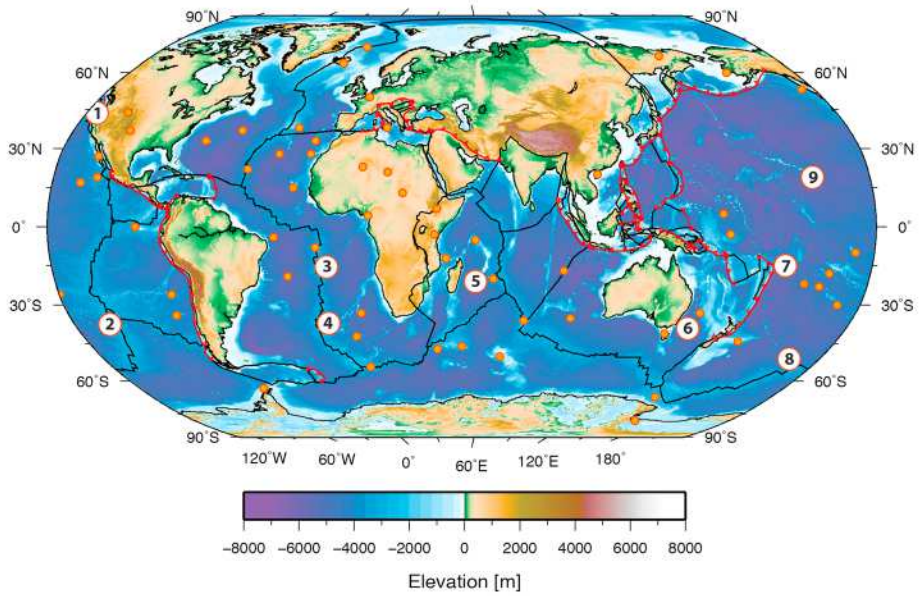

Figure 1. Present-day distribution of global tectonic features. White numbered circles indicate approximate present-day location of hotspots used in this study: (1) Cobb, (2) Foundation, (3). St. Helena, (4) Tristan, (5) Réunion, (6) Tasmantid, (7) Samoa, (8) Louisville, and (9) Hawaii. Approximate present-day locations of hotspots are marked with small orange circles (Doubrovine et al., 2012; Knesel et al., 2008; Koppers et al., 2012; McDougall & Duncan, 1988; O'Connor et al., 2013; O'Neill et al., 2005; Wessel & Kroenke, 2008). Subduction zones are marked in red with triangles indicating dip direction, and solid black lines indicate mid oceanic ridges and transform faults (Müller et al., 2016). Tectonic features overlay ETOPO1 (Amante & Eakins, 2009).

approximately stationary over geological timescales. Published APM models typically fall into one of two categories: mantle-derived or spin axis-derived reference frames.

2. Absolute Reference Frames

Mantle reference frames, particularly since the Cretaceous, generally rely on the analyses of hotspot trails, the result of a time-dependent interaction between hot mantle upwelling plumes and the respective overriding plate. These interactions manifest themselves on the seafloor as linear chains of volcanic activity displaying a recognizable age progression and geometry proportional to the motion vector of the overriding plate (Morgan, 1971; Muller et al., 1993; O'Neill et al., 2005; Torsvik, Steinberger, et al., 2008; Wilson, 1963). As plumes (and thereby hotspots) move laterally approximately an order of magnitude slower than plates (O'Neill et al., 2005; Stock & Molnar, 1982), for the development of APM models they can either be considered fixed in place over geological time (Maher et al., 2015; Morgan, 1971; Muller et al., 1993; Wessel & Kroenke, 2008; Wilson, 1963) or permitted to move independently with respect to each other and the mantle (Doubrovine et al., 2012; O'Neill et al., 2005; Steinberger et al., 2004). Notwithstanding this key uncertainty, due to a concentration of observations from more recent geological time, hotspot APM models are considered most robust for the past ~80 Myr.

To address this limitation, correlations between the surface geological record and features identified in seismic tomographic imaging have been proposed. Assuming slab material sinks vertically, van der Meer et al. (2010) utilized a global mantle tomographic model to identify candidate remnant subducted oceanic plates within the lower mantle and reconstructed them back to the orogenic zones they likely originated from, yielded estimates of slab sinking rates. From this, a global average constant sinking rate was derived and used to longitudinally shift the plate model, by "slab fitting." Due to improved understanding of variations in slab sinking rates (van der Meer et al., 2018; Wang et al., 2018), limitations in tomographic modeling, and slab survival times in the mantle (van der Meer et al., 2010, 2018), this "slab fitting" method is valid for the past 300 Myr at most. Further back in time, a long-term correlation between Large Low Shear Velocity Provinces (LLSVPs), thermochemical density anomalies identified by seismic studies in the lower mantle,

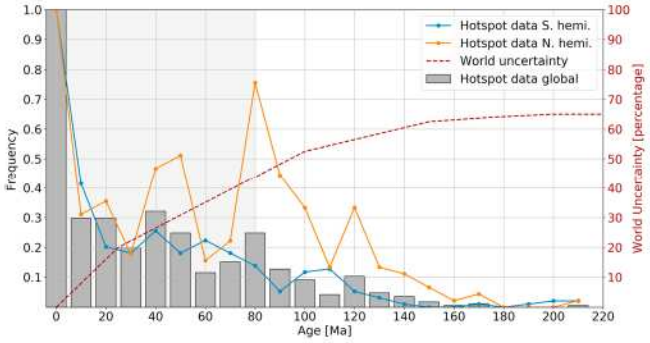

Figure 2. Time-dependent availability of hotspot data typically used to constrain plate reconstructions normalized to present-day frequency. Gray bars are the relative global number of age-dated hotspot trail observations, with blue and orange lines representing the relative availability of age-dated hotspot trail observations split by hemisphere. Red dashed line is estimated "world uncertainty" representing the percentage of lithosphere subducted since a given time (Müller et al., 2016) following Torsvik et al. (2010) and Torsvik and Cocks (2016). The light gray background color spanning 80–0 Ma represents the period from which age-dated hotspot trail data were used in this study.

and the reconstructed eruption locations of Large Igneous Provinces and kimberlites as observed at the surface of the Earth has been proposed (Burke et al., 2008; Steinberger & Torsvik, 2008; Torsvik et al., 2006; Torsvik, Steinberger, et al., 2008). This suggested correlation may present a long-term link between surface motions and a fixed mantle reference frame is proposed to potentially persist for 300 Myr or more (Torsvik, 2018). Similar to hotspot fixity, understanding and ultimately constraining the absolute motions of the LLSVPs themselves remains a challenge, with geodynamic studies producing a wide range of LLSVP stability scenarios (Deschamps & Tackley, 2008, 2009; *Flament* et al., 2017; McNamara & Zhong, 2004, 2005; Tan & Gurnis, 2005, 2007).

Geodynamic investigations into the relationship between seismic anisotropy in upper mantle and seafloor spreading directions at active ridges provide an alternative set of observations to produce a global seafloor spreading aligned reference frame for present day (Becker et al., 2015), but the physical basis of this correlation remains obscure. Further investigation into this potential correlation extended back in time by Wessel and Müller (2016) and Williams et al. (2016) found that the first-order alignment between spreading direction and absolute motions appeared to be time dependent, correlating back to ~20–30 Ma, but was inconsistent globally. Alternatively, data implying a fixed relationship to the spin axis such as paleomagnetic observations can be used to constrain absolute motions (Mitchell et al., 2012; Schettino & Scotese, 2005; Steinberger & Torsvik, 2008; Torsvik et al., 2012). Assuming the geocentric axial dipole (GAD) model and given a sufficient geological window, the time-averaged locations of Earth's magnetic poles approximate the locations of the spin axis, and a fixed absolute relationship exists between the location of the paleomagnetic source rock and the location of the magnetic poles at the age of magnetization (Butler, 1991; Tauxe, 2010). When data from two or more continents are considered together, this relationship can be used to derive both relative and APMs. As paleomagnetic data are vector quantities, potentially containing an unknown proportion of primary remanent magnetization and the localized realization of a global true polar wander (TPW) component, which is itself difficult to quantify due to the nonuniqueness of the problem, and the uncertain geological and geodynamic assumptions required to derive realistic TPW estimates, they require complex processing and are vulnerable to systematic error (Evans, 2003; Tsai & Stevenson, 2007; Steinberger & Torsvik, 2008; Torsvik et al., 2012; Torsvik et al., 2017).

In this study, we present an alternative approach to reconstructing APMs over the last 220 Myr of Earth history. Through the joint global inversion of multiple constraints including hotspot location and associated trail data, paleomagnetic observations, global trench migration (TM) behavior, and estimates of NLR, we seek to explore the global solution space to identify the optimal absolute motions of a given reference plate in a hierarchical plate model producing relative motions with the closest global fit to observations. We investigate the relative sensitivities and global constraining abilities of each data type and compare these results with a diverse suite of published APM models, including an evaluation of APM models produced for times when hotspot data are not available.

3. Data Constraints and Uncertainty Considerations

Constraining global absolute motions using all available data is difficult, primarily due to the imperfect nature of geological and geophysical data, characterized by unequal spatial and temporal global sampling distributions (Figure 2). For example, the volcanic trails used to constrain hotspot reference frames are mostly found on oceanic lithosphere, which is less frequently preserved back in time. It is estimated that the "world uncertainty," that is, the amount of lithosphere that has been subducted since a given time and is subsequently unavailable for use as a constraint in tectonic reconstructions is as high as 60% by ~140 Ma and 65% by ~220 Ma (Müller et al., 2016) following Torsvik et al. (2010) and Torsvik and Cocks (2016). Estimated world uncertainty is anticorrelated with preservation of hotspot chain data (Figure 2). Further, hotspot trails are not evenly distributed across the different plates—for example, the African and Pacific

plates host multiple trails commonly used for APM modeling, while the Eurasian plate hosts none, with the track associated with the Iceland hotspot, itself located on the axis of the Mid-Atlantic Ridge, located on the North American plate. The rate at which plumes move within the mantle remains debated (Wang et al., 2017), and estimating the independent motions of hotspots is prone to significant uncertainties due to the current knowledge of mantle properties and paleogeography, together with the extremely limited set of observations independently constraining hotspot motions (Doubrovine et al., 2012; O'Neill et al., 2005; Steinberger, 2000; Steinberger et al., 2004). Quantitatively assessing uncertainty in alternative data sets to hotspots, such as those using the history of subduction preserved in the geological and geophysical record (van der Meer et al., 2010; Williams et al., 2015) present a similar challenge. To account for these and other complications including computational limitations, models are simplified. This is most often achieved by constraining motions using a single data source to avoid conflicts, such as hotspot trails or paleomagnetic data, and by incorporating some basic assumptions as to the expected tectonic behavior such as fixity of hotspots or LLSVPs, or vertical sinking of slab material though the mantle. As a direct result of these model parameter selections, coupled with the choice of RPM model used, a wide range of valid end-member models are produced displaying very different behaviors with respect to TM and net rotation rates (Williams et al., 2015). Assessing and comparing the spectrum of available models is challenging, since competing models appear to fit their respective data sources within the associated uncertainties. In this study we aim to find a generalized global solution taking multiple data types into account, using a joint inversion approach constrained by simultaneously meeting the criteria of three global data constraints—hotspot trail observations, subduction zone kinematics, and NLR. We investigate variable weightings of these constraints using two published RPM models (Müller et al., 2016; Shephard et al., 2013), creating a suite of end-member APM models from 220–0 Ma and independent absolute hotspot motion models from 80–0 Ma.

3.1. Relative Plate Motion Models

For our method, a global topological or "full plate" tectonic model is required. Models are categorized as topological only if they combine RPMs with an explicitly defined continuous and self-consistent global set of closed polygons describing the global distribution of plates coupled with independently located, identified and mobile plate boundaries through time (Gurnis et al., 2012; Seton et al., 2012; Müller et al., 2016; Merdith et al., 2017; Müller et al., 2019). Global RPMs are extracted and used in this analysis (all existing reference frames from the published models are removed), from two published kinematic plate reconstructions representing alternative global plate motion scenarios, referred to as S13 and M16, respectively (Müller et al., 2016; Shephard et al., 2013). Model S13 is an extension of the global Seton et al. (2012) reconstruction with updated plate kinematics and geometries in the circum-Arctic, specifically formation of the Wrangellia Superterrane prior to ~140 Ma and the evolution of the Amerasia basin at ~120 Ma. The M16 model builds on both the Seton et al. (2012) and the Shephard et al. (2013) models with the integration of a number of recently published regional models primarily updating the behaviors of the North and South Atlantic, Labrador Sea, Caribbean, Indian Ocean, Pacific Ocean, and North America, with updated plate relationships between the Indo-Atlantic and the Pacific (Müller et al., 2016). The use of two alternative plate models to test different plate motion scenarios is motivated from the recognition of a key uncertainty present in global relative plate models related to the difficulty in directly relating the plate motions of the Indo-Atlantic and Pacific domains. This uncertainty makes global plate behavior highly sensitive to the chosen plate circuit in a given model and is a suitable end-member test of the ability of an APM model to constrain global plate motions from a single reference (Gordon & Jurdy, 1986; Schellart et al., 2006; Matthews et al., 2011). The choice of RPM model also has a strong impact on the ability of the APM inversion to converge on best fitting solutions to models constrained by given data types. This is most apparent in global APM models constrained using hotspot trail data as the relative motion of the Indo-Atlantic with respect to the Pacific greatly affects global fits for times younger than ~80 Ma (as opposed to more conventional approaches of calculating APM models for the Indo-Atlantic and Pacific independently; Muller et al., 1993; Wessel & Kroenke, 2008). Other global constraints such as TM behavior are minimally affected by relative Indo-Atlantic/Pacific motion; however, they are influenced by differences between the S13 and M16 models in terms of the subduction histories in certain regions.

Relative motion between individual plates are derived by analyzing seafloor magnetic anomalies in conjunction with global seafloor age grids (Müller et al., 1997). Individual motions are represented by Euler

poles (latitude, longitude, and rotation angle) and are computed by rotating identified anomalies using great circle arcs following fracture zone orientations (Hellinger, 1981). Individually calculated relative rotations are tied to global relative rotations using a hierarchical inverted tree structure via a defined plate circuit, with an identified "reference plate" at the top (Müller et al., 2016; Seton et al., 2012; Shephard et al., 2013). For use with relative motion models, the choice of reference plate is somewhat arbitrary, only requiring an established connection to all major plates via the selected plate circuit and ideally demonstrating minimal motion throughout the period of interest. For these reasons, the African plate is typically used as a reference for Mesozoic and younger times, as is the case in both S13 and M16, due to its central location within the supercontinent Pangea, as it was surrounded by mid-ocean ridges at the time of continental breakup limiting longitudinal motion (Torsvik, Müller, et al., 2008). Quantifying the overall uncertainties associated with values such as net rotation and TM in global RPM models is difficult, as the construction of these models is an iterative process integrating many different quantitative and qualitative data types from many independent studies. Combined with a non-uniform sampling density of data across the globe, this produces a model where not all regions are equally constrained or have calculated uncertainties associated with them. For our purposes, we do not explicitly incorporate uncertainties related to the relative motion model into the optimization algorithm. Instead, we investigate results for two alternative topological plate models which, though identical in many respects, contain important differences reflecting differing regional interpretations of plate motions and subduction histories. This provides a useful indication of how choices in the input plate reconstruction can influence the resulting APM results.

3.2. Plume Locations and Hotspot Trail Data

As detailed in section 2, hotspot trail observations are a key data set for evaluating APMs for times where hotspot related volcanism found in present-day seafloor has been extensively studied. In this analysis, we use a global data set containing nine well-studied present-day hotspot locations, each with associated hotspot trail geometries located wholly within a plate and consistent age progressions for times since 80 Ma from (1) Cobb, (2) Foundation, (3) St. Helena, (4) Tristan, (5) Réunion, (6) Tasmantid, (7) Samoa, (8) Louisville, and (9) Hawaii (Figure 1; McDougall & Duncan, 1988; O'Neill et al., 2005; Knesel et al., 2008; Wessel & Kroenke, 2008; Doubrovine et al., 2012; Koppers et al., 2012; O'Connor et al., 2013). A number of geological and geophysical uncertainties are associated with the use of hotspot data in global plate reconstructions. The primary sources of error originate from the accurate identification of the present-day position of a given hotspot that is assumed to have formed the chain (or predicted past position if the hotspot is no longer active) and the uncertainty of the associated seafloor volcanism reconstructed through time using this assumption. An additional source of uncertainty comes from the simplifying assumption that the location of surface volcanism is directly correlated with the location of the plume head "centroid," producing a predictable monotonically increasing age/distance relationship along the chain (e.g., O'Neill et al., 2005; Torsvik, Müller, et al., 2008; Wessel & Kroenke, 1998). A number of published estimates ranging between ~10 and 30 mm/year exist for the potential rate of both absolute and relative hotspot motion globally, with varying levels of reported fit to observed oceanic hotspot tracks (Doubrovine et al., 2012; Koivisto et al., 2014; O'Neill et al., 2005; Wang et al., 2017). To calculate the optimal reference frame rotation for a given time in this study, global hotspot locations are treated as fixed in place over their respective lifetimes, with the expected resulting hotspot trail misfit modeling estimates of independent absolute hotspot motion (Divenere & Kent, 1999; Hassan et al., 2016; Koppers et al., 2004; Koppers et al., 2011; Koppers et al., 2012; Molnar & Atwater, 1973; Molnar & Stock, 1987; Tarduno et al., 2003). To improve computational efficiency and remove any potential for bias created by the non-uniform sampling both along and between different trails, all trail data were interpolated at 5-Myr intervals. Following the findings of Hoernle et al. (2015), only observations associated with the Tristan track (and not the Gough Track) for sample ages <71 Ma were included. Evaluation of hotspot trail misfit proposed in APM models during inversion is calculated by the along-strike great circle distance mismatch between a predicted and observed hotspot location at a given time and the hotspot location at the previous time step with a fit threshold of 50 km to account for hotspot paleolocation uncertainties. The great circle distance d between two points is calculated using

$$d = 2r\ \sin^{-1}\left(\sqrt{\left(\frac{\phi_2-\phi_1}{2}\right) + \cos(\phi_1)\ \cos(\phi_2)\ \sin^2\left(\frac{\lambda_2-\lambda_1}{2}\right)}\right) \quad (1)$$

where r is the radius of the Earth, φ_1 and φ_2 are the latitude of point 1 and latitude of point 2 in radians, and λ_1 and λ_2 are the longitude of point 1 and longitude of point 2 in radians. The along-strike hotspot trail misfit HS_m is calculated using

$$HS_m = \sum_{i=0}^{n} (d_{1i}-d_{2i})^{-1} + HS_{gm}\sigma \quad (2)$$

where d_{1i} is the predicted along-strike great circle distance between time T_i and T_{i-1}, d_{2i} is the observed along-strike great circle distance between observations at T_i and T_{i-1}, and $HS_{gm}\sigma$ is the global hotspot trail misfit standard deviation.

3.3. Subduction Zone Kinematics

The quantification of global kinematic subduction behavior within plate models is a conceptually simple yet powerful approach to evaluate alternative plate reconstructions. To the first order, it is to be expected that any modeled global plate motions (assuming the plate reconstruction model is complete and self-consistent, Gurnis et al., 2012) produce global subduction zone kinematics that are both tectonically and geodynamically plausible (Becker, 2006; Conrad & Behn, 2010; Gurnis et al., 2012; Schellart et al., 2008; Williams et al., 2015). As subduction zones are represented as discrete noncontinuous objects within a RPM model, calculations of trench behavior are relatively independent from the global plate system, making them minimally affected by uncertainties relating to the chosen RPM plate chain. The primary source of uncertainty of subduction zone data in geologically informed geometric RPM models such as S13 and M16 comes from reconstructions of trench location, geometry, and subduction polarity. The quantitative spatial error associated with each of these parameters, similar to the estimated lateral spatial root-mean square (RMS) uncertainty of 250–500 km presented in van der Meer et al. (2010), is both difficult to define due to the qualitative nature of the reconstructions and likely to propagate back through time as models are constrained by increasingly sparse observations (Schellart et al., 2008; Williams et al., 2015). In this study, trench kinematics are calculated following the method outlined in Williams et al. (2015). Topologically closed global plate boundaries are extracted at 1-Myr intervals from 220–0 Ma from each RPM model using the software *GPlates* (Boyden et al., 2011). From these, global subduction zones are further extracted and sampled along strike in 1-arc degree segments. During the inversion, at each iteration the absolute TM velocity vectors orthogonal to local trench geometry are calculated for each segment (Kaula, 1975; Lallemand et al., 2008; Schellart et al., 2008). From these sets of vectors, single quantities descriptive of global subduction behavior are calculated including rates, frequencies, and variance of both trench advance and retreat (Schellart et al., 2008), generating a global subduction kinematic snapshot representing the combination of given RPM and APM models for a single point in time. During the inversion process, proposed APM models are evaluated by subduction zone kinematics using

$$TM_k = \frac{\Sigma|V_T|}{T_n} + TM_{gT}\sigma \quad (3)$$

where TM_k is the nondimensional value representing calculated trench kinematics, $|V_T|$ is the global trench-normal velocity vector, $TM_{gT}\sigma$ is the global trench-normal velocity standard deviation, and T_n is the total number of trench segments. This approach is designed to converge on models that minimize global trench-normal velocities (Schellart et al., 2008).

3.4. Net Lithospheric Rotation

Estimates of mean NLR rates from modeling suggest a wide range of geodynamically plausible values. Geodynamic flow models provide the lowest estimates of NLR ranging from 0.06–0.15° Myr (Becker, 2006; Becker & Faccenna, 2011; Zhong, 2001), with Conrad and Behn (2010) suggesting global azimuthal anisotropy constrains NLR to an upper bound of ~0.26°/Myr. Models incorporating hotspot data produce the greatest variance ranging from 0.13–0.44°/Myr (Cuffaro et al., 2007; Gripp & Gordon, 2002; O'Neill, 2005; Steinberger et al., 2004; Torsvik et al., 2010). Based on the wide range of findings of these studies which

can be interpreted as representing experimental uncertainty of the mechanics controlling differential rotation of the lithosphere and the underlying mantle, NLR is applied as a constraint in the optimization workflow with the following two assumptions: (1) Lower rates of net rotation, in particular those within the bounds placed by the modeling studies mentioned above, can be considered more likely, and (2) NLR magnitude is not expected to be zero. NLR magnitude and associated Euler pole are calculated after the approach detailed in Torsvik et al. (2010) using

$$\omega_{\text{net}} = 3/\left(8\pi r^4\right)\Sigma_i \int (\omega_i \times R) \times R \mathrm{d}S_i \tag{4}$$

where ω_{net} is the calculated NLR rate in degrees per million years, r is the radius of the Earth, R is the plate rotation velocity vector, dS is the area element integrated over the sphere, and ω is the plate angular velocity vector for a given plate. Sampling at a spatial resolution of ~50 km, NLR is calculated globally at 2-Myr intervals then time averaged to match the APM time steps of 10 Myr and evaluated against a precomputed no net rotation version of the RPM models to isolate an approximate rate of NLR present in each proposed model.

4. Model Setup

APM models produced in this study seek to identify the optimal absolute motions of the reference African continent in 10-Myr stages spanning from 220 Ma to present day. The optimal solutions seek to fit observations along hotspot trails while also maintaining reasonable values for NLR and quantities describing global TM characteristics. The unknown best fitting Euler rotation parameters (latitude, longitude, and rotation angle) for southern Africa are found via an iterative direct search optimization algorithm. The algorithm is a version of Powell's implementation of the COBYLA (Constrained Optimization BY Linear Approximations) derivative-free direct search algorithm (Powell, 1994, 1998, 2007), as implemented in NLopt (Johnson, 2016). For each time step, an initial Euler rotation is required from which the iterative search algorithm can progress toward a minimum. As paleomagnetic data represent the absolute location of sampled rocks at a point in time, they are ideal to derive the initial reference position for Africa. The paleomagnetic data implementation is designed to avoid any bias that may be introduced by using precalculated or published reference positions of Africa derived from multiple data types or existing preprocessing methods. A simple APM model for southern Africa from 248.5 Ma was constructed from compiled paleomagnetic pole data (Torsvik et al., 2012) (using only data with a Van der Voo, 1990, quality criteria score of $Q \geq 3$), with finite Euler rotations computed at 10-Myr intervals (Table 1). Although individual poles have both age and calculated geographical uncertainties (A95) associated with them, these are not explicitly incorporated. Individual poles are assigned a mean age and are used strictly as nucleation points to generate the geographic model suite starting distribution, which itself is larger than the A95 ellipse. This reasoning is also applicable to potential existence of a TPW signal within the paleomagnetic data used to generate the starting distribution. To fully explore the solution space and avoid the potential for nonconvex convergence to local minima, a random distribution of alternative starting finite rotations is generated from the initial paleomagnetic starting rotation, which acts as the nucleus. These are then projected onto the surface of a sphere within an ellipse of radius 30° centered on the paleomagnetic starting rotation as it is assumed that the paleomagnetic data provide a sufficiently accurate starting rotation that is likely close to the optimal solution. As the optimization algorithm spatial search extents exceed the range of maximum estimated magnitudes of possible TPW at each time step, coupled with large variation in published estimates of TPW magnitudes, timing, and behavior as a result of varying geodynamic assumptions and time-dependent plate configurations, paleomagnetic seed data were implemented within the method without explicit TPW correction (Evans, 1998; Evans, 2003; Kirschvink, 1997; Li et al., 2004; Li & Zhong, 2009; Mitchell et al., 2012; Torsvik et al., 2012).

From initial testing, it was found that the generation of 100 alternative starting rotations, and associated distributions for each time step was sufficient to converge to a result representative of the unknown global minimum, with further inversions failing to produce significantly better fitting results. As each starting rotation represents the initial condition for a discrete inversion, and as there is no interdependency between inversions, this approach is suitable for a parallel workflow (Herlihy & Shavit, 2012), experiencing near to linear scaling with the addition of more CPU cores.

Table 1
Paleomagnetic Pole Data Used to Construct Southern Africa Motion Model Taken From Torsvik et al. (2012)

Q	A95	*k*	*N*	Age	Formation	S Lat/Lon	P Lat/Lon	Ref.
5	5.2		118	90.5	Cretaceous Kimberlites 1, South Africa, Lesotho	−29/26	−64.1/46.1	2293
6	9.7		100	129	Cretaceous Kimberlites 2, South Africa	−28.5/24	−47.6/89.9	2293
5	3.1	53.3	118	132	Kaoko lavas, Namibia	−20/14	−48.3/86.6	126
4	13.3	33.9		180	Batoka basalts, northern Zimbabwe	−17.9/26.2	−64/80.6	Jones et al. (2001)
3	15.8	62.2	10	183	Hoachanas lavas, Namibia	−24/18	−61.9/71.9	126
5	3.2	42.1	292	183	Stormberg lavas (Lesotho basalts), South Africa	−29.3/28.6	−71.6/93.5	3090
4	11	70.2	74	183	Stormberg lavas, Sani Pass and Maseru, Lesotho	−29.5/28.5	−70.5/88.7	984
3	7		32	183	Karroo lavas, Central Africa, Zimbabwe, Mozambique	−18/30	−57/84	635
5	9.5		67	183	Karroo dolerites combined, South Africa, Zimbabwe	−24/31	−65.4/75.1	317
5	8.7	41.3	68	186	Marangudzi Ring Complex, Zimbabwe	−22.1/30.7	−70.7/106.7	470
3	4.6	208	32	221.5	Red sandstone Formation, Zambia[a]	−16.2/28.8	−54.7/39.5	323
3	6	21	25	248.5	Cassanje Series, Angola[a]	−10/17.5	−49/62.6	1960

Note. *Q* is the Van der Voo quality factor (Van der Voo, 1990), *A95* is the pole 95% confidence limit, *k* is the Fisher kappa statistic of dispersion, *N* is the number of samples, S Lat/Lon is the sample site latitude and longitude, P Lat/Lon is the calculated pole latitude and longitude, and *Ref.* is the pole reference in the Global Paleomagnetic Database (GPMDB) where available.
[a]Poles with an inclination shallowing correction of $f = 0.6$ applied as per Torsvik et al. (2012).

4.1. Optimization Process and Objective Function

For each 10-Myr stage, a given starting finite Euler rotation is generated from the reference paleomagnetic model for southern Africa. The optimization algorithm iteratively perturbs the starting finite rotation latitude, longitude, and rotation angle values and evaluates if the newly proposed model better satisfies our chosen criteria. To do this, an objective function is required to evaluate the proposed solutions. The objective function within this framework performs two operations per iteration: First, it takes the newly proposed finite rotation for southern Africa, inserts this into the given RPM model within memory, and using the software *pyGPlates*, an application programming interface (API) designed for *GPlates* (Boyden et al., 2011; Müller et al., 2018), recalculates the global APMs with the proposed southern Africa poles, generating a new candidate global plate model. To evaluate the proposed model, the objective function calculates the total "cost" of the model, which is descriptive of and represents the "goodness of fit" of the model to the expectations of prescribed data constraints (section 3). The total cost J is calculated using

$$J = \frac{HS_m}{\sigma_1} + \frac{TM_k}{\sigma_2} + \frac{\omega_{\text{net}}}{\sigma_3} \tag{5}$$

where HS_m (equation (2)) is the calculated global hotspot trail misfit, TM_k (equation (3)) is the calculated global TM kinematics value, ω_{net} (equation (4)) is the calculated rate of NLR, with σ_1, σ_2, and σ_3 the relative weightings for each constraint. As this is a minimizing function, if the returned cost for a given iteration is lower than the previous iteration—that is to say the rotation pole proposed in the given iteration produces an improved global "fit" to constraints—then the algorithm will proceed along this trajectory iteratively reducing the cost by proposing similarly perturbed finite rotation poles toward a model minima. Alternatively, if the resulting fit evaluation returns a larger value than the previous attempt, the next step will be in a new direction in an attempt to identify the "downhill" trajectory toward the model minima (Figure 3). This iterative approach continues until the algorithm reaches a minima and is unable to minimize the global fit any further by stepping in any direction, at which time the optimal finite rotation pole is returned. Of the 100 optimized APM models run at each time step, the model with the smallest cost is selected as most closely approximating the global minima and incorporated into the optimal APM model moving backward in time.

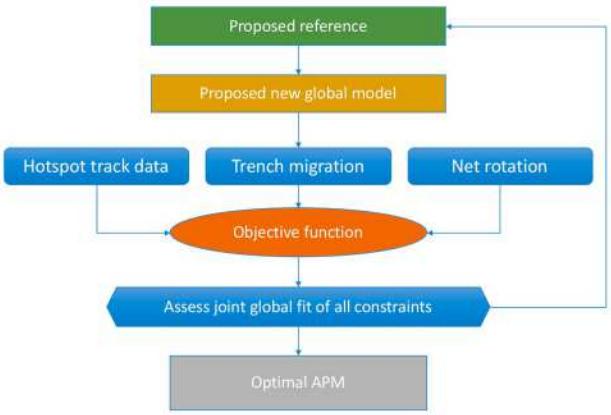

Figure 3. Schematic representation showing the iterative nature of the optimization method workflow from initial proposed reference frame to optimized absolute plate motion.

Table 2
List of APM Models Produced in This Study With Relative Constraint Weightings

Model name	Period (Ma)	Constraints (weighting)
OptAPM1-M16*, OptAPM1-S13**	**80–0**	$\boldsymbol{HS_m(1),TM_k(1),\omega_{net}(1)}$
OptAPM2-M16, OptAPM2-S13	80–0	$HS_m(0.5),TM_k(1),\omega_{net}(1)$
OptAPM3-M16, OptAPM3-S13	80–0	$HS_m(1),TM_k(0.5),\omega_{net}(1)$
OptAPM4-M16, OptAPM4-S13	80–0	$HS_m(1),TM_k(1),\omega_{net}(0.5)$
OptAPM5-M16*, OptAPM5-S13**	**220–0**	$\boldsymbol{TM_k(1),\omega_{net}(1)}$
OptAPM6-M16, OptAPM6-S13	220–0	$TM_k(0.5),\omega_{net}(1)$
OptAPM7-M16, OptAPM7-S13	220–0	$TM_k(1),\omega_{net}(0.5)$
OptAPM8-M16, OptAPM8-S13	220–0	$TM_k(1)$
OptAPM9-M16*, OptAPM9-S13**	**220–0**	$\boldsymbol{\omega_{net}(1)}$

Note. HS_m is the along-strike hotspot trail misfit, TM_k are the calculated trench migration kinematics and ω_{net} is net lithospheric rotation. RPM model *M16* = Müller et al. (2016), *S13* = Shephard et al. (2013). Models denoted with * constitute the preferred suite of results with models denoted in bold discussed in the main text. Euler rotations for each model are provided in Table S1 found in the supporting information.

5. Results and Discussion

To explore the relative influence and ability of each constraint to resolve geodynamically reasonable APMs, a total of nine alternative optimized global APM models representing a number of end-member scenarios was derived from each RPM model. Each model explores different combinations of constraints and independent constraint weightings, together building a suite with a total of 18 alternative APM models spanning from 80–0 Ma for models including hotspot data, and from 220–0 Ma for models excluding hotspot data (Table 2), with Euler rotations for all models provided in Table S1 in the supporting information. Resulting APM models of selected optimized APM models calculated using Müller et al. (2016) are discussed in this section, with optimized APM models derived using Shephard et al. (2013) provided in the supporting information (Table S1). To evaluate the performance of the resulting optimized APM models, we compare them to six published APM models, each applied to the same RPM, by calculating a standard set of metrics for each with the aim of characterizing a range of tectonic behaviors predicted by each plate model (APM + RPM). For each APM model tested with a given metric, a score is calculated to rank the statistical performance of the given model relative to the other APM models tested. Individual metric testing scores are subsequently summed to provide a final ranking of the APM models used in this study, with lower scores representing optimal statistical performance (Tables 3–5, Table 6).

Following the widely used convention adopted by previous studies (Müller et al., 2016, 2019; Seton et al., 2012; Torsvik et al., 2012), to effectively constrain the absolute motions of a given global plate motion model, a fixed reference point on the surface of the Earth from which all plates move relative to must be established. Dependent on the type of data used to derive the APM and the way the RPM model is setup, this reference point can be Earth's spin axis (when using paleomagnetic data), long-lived mantle features that can be tied to a point on the surface through time (in the case of hotspot trail observations and mantle tomography), the subtraction of NLR from the model, or any combination thereof. In the case of both the RPM models used in this study, southern Africa is used as a reference plate, itself moving relative to the spin axis, and all other plates in an "inverted tree" hierarchical structure moving relative to southern Africa (Müller et al., 2016). As a result of this model setup, calculated motion paths of southern Africa can be used as a way of visualizing and comparing alternative APMs as their primary goal is to constrain the motion of the reference plate. A series of calculated paths describing the motion of southern Africa generated using the preferred APM models from this study and six alternative published APM models each applied to the same RPM model taken from Müller et al. (2016) shows that plate reconstructions are sensitive to the APM model used and the data and methods from which it is constrained (Figure 4).

As southern Africa is used as the reference plate in both S13 and M16, variations of latitude and longitude of up to >10° since the Late Cretaceous, like those shown from Doubrovine et al. (2012), herein referred to as D2012 using hotspot data, and Torsvik et al. (2012), herein referred to as T2012 using paleomagnetic data, can propagate through the entire plate circuit producing different plate motion models. It is

Table 3
Global APM Model RMS Velocity Statistics in Millimeters per Year Sorted by Mean ($\bar{x}$)

APM model	η	Age	Min	Max	$\bar{x}$	M	G_σ^2	$\sum G$	σ	Score
OptAPM1-M16	***8681***	***80–0***	***15.14***	***64.38***	***31.88***	***26.26***	***0.05***	***79.77***	***14.57***	***11***
OptAPM5-M16	***8681***	***80–0***	***15.53***	***64.62***	***31.99***	***26.1***	***0.05***	***79.73***	***14.68***	***10***
OptAPM9-M16	***8681***	***80–0***	***15.49***	***64.92***	***32.1***	***26.13***	***0.05***	***79.71***	***14.8***	***13***
T2008	8681	80–0	14.71	63.51	**33.04**	26.73	0.11	79.91	14.74	21
V2010	8681	80–0	14.11	72.51	**34.42**	31.55	0.12	80.3	16.5	29
O2005	8681	80–0	14.37	73.78	**34.46**	30.32	0.55	82.18	17.73	35
D2012	8681	80–0	11.74	81.36	**36.88**	29.99	0.14	81.74	20.23	34
T2012	8681	80–0	19.44	77.19	**40.5**	36.24	0.03	78.78	17.08	24
OptAPM5-M16	***8681***	***120–0***	***11.88***	***74.09***	***33.03***	***27.78***	***0.06***	***123.09***	***16.81***	***8***
OptAPM9-M16	***8681***	***120–0***	***11.38***	***75.11***	***33.24***	***27.89***	***0.06***	***123.13***	***17.13***	***12***
T2008	8681	120–0	8.42	75.39	**34.82**	30.28	0.09	122.73	19.5	18
V2010	8681	120–0	11.38	77.81	**34.93**	28.95	0.11	123.83	17.77	21
D2012	8681	120–0	8.88	87.82	**38.43**	35.39	0.21	124.44	21.9	28
T2012	8681	120–0	14.95	83.46	**39.16**	35.57	0.05	121.88	17.68	17
OptAPM5-M16	***8681***	***220–0***	***5.59***	***74.92***	***28.73***	***25.66***	***0.11***	***225.22***	***16.47***	***8***
OptAPM9-M16	***8681***	***220–0***	***5.57***	***76.01***	***29.07***	***26.28***	***0.1***	***225.35***	***16.77***	***11***
S2008	8681	220–0	6.19	83.76	**36.17**	32.38	0.23	227.83	19.41	19
T2012	8681	220–0	8.73	91.61	**36.62**	33.13	0.08	224.68	19.79	14
V2010	8681	220–0	8.04	88.28	**37.59**	34.03	0.15	227.3	19.93	23

Note. APM model = absolute plate motion model, η = number of samples, Age = age range for comparison in million years, Min = global minimum velocity, Max = global maximum velocity, $\bar{x}$ = global arithmetic mean velocity, M = global median velocity, G_σ^2 = global velocity gradient variance (GVGV), $\sum G$ = sum of global velocity gradients, σ = global velocity standard deviation and *Score* = nondimensional sum of column ranks for $\bar{x}$, M, G_σ^2, $\sum G$, and σ with a lower score representing higher overall statistical ranking within age category. Models denoted in bold italics discussed in the main text. Mean values for all models denoted in bold. A full table containing RMS statistics for all APM models can be found in the supporting information.

acknowledged that each of these APM models was derived using slightly different RPM models, none of which were S13 or M16, so making any direct comparisons between APM models applied to a single alternative RPM model remains approximate; however, as the RPM model used in each of the alternative

Table 4
Global Net Lithospheric Rotation Statistics in Degrees per Million Years Sorted by Magnitude Arithmetic Mean

APM model	Age	Min	Max	$\bar{x}$	M	$G_\sigma^2 \times 10^3$	$\sum G$	σ	*Score*
OptAPM9-M16	***80–0***	***0.005***	***0.108***	***0.042***	***0.042***	***0.043***	***5.020***	***0.032***	***9***
OptAPM5-M16	***80–0***	***0.006***	***0.108***	***0.043***	***0.043***	***0.039***	***5.020***	***0.032***	***10***
OptAPM1-M16	***80–0***	***0.005***	***0.108***	***0.047***	***0.047***	***0.026***	***5.020***	***0.032***	***11***
T2008	80–0	0.072	0.203	**0.146**	0.155	0.193	4.993	0.039	18
V2010	80–0	0.055	0.357	**0.166**	0.155	0.498	5.032	0.096	31
O2005	80–0	0.078	0.442	**0.174**	0.100	0.999	5.029	0.121	30
D2012	80–0	0.106	0.331	**0.200**	0.156	0.220	5.029	0.086	27
T2012	80–0	0.158	0.457	**0.302**	0.323	0.974	5.019	0.092	30
OptAPM9-M16	***120–0***	***0.005***	***0.108***	***0.059***	***0.054***	***0.038***	***9.020***	***0.034***	***6***
OptAPM5-M16	***120–0***	***0.006***	***0.108***	***0.061***	***0.055***	***0.033***	***9.020***	***0.035***	***7***
T2008	120–0	0.072	0.360	**0.206**	0.174	0.206	9.035	0.089	17
V2010	120–0	0.055	0.438	**0.228**	0.171	0.966	9.073	0.132	24
D2012	120–0	0.106	0.575	**0.272**	0.280	0.651	9.026	0.134	24
T2012	120–0	0.158	0.545	**0.379**	0.352	0.633	9.056	0.127	25
OptAPM9-M16	***220–0***	***0.005***	***0.108***	***0.047***	***0.043***	***0.052***	***19.000***	***0.033***	***5***
OptAPM5-M16	***220–0***	***0.006***	***0.108***	***0.049***	***0.047***	***0.052***	***19.000***	***0.034***	***8***
S2008	220–0	0.063	0.401	**0.206**	0.178	0.606	19.044	0.098	16
V2010	220–0	0.055	0.438	**0.236**	0.237	1.303	19.067	0.129	22
T2012	220–0	0.111	0.545	**0.335**	0.348	1.106	19.027	0.133	22

Note. APM model = absolute plate motion model, Min = global minimum net lithospheric rotation (NLR) magnitude, Max = global maximum NLR magnitude, $\bar{x}$ = global arithmetic mean NLR magnitude, M = global median NLR magnitude, $G_\sigma^2 \times 10^3$ = scaled global NLR magnitude gradient variance (GMGV), $\sum G$ = sum of global NLR magnitude gradients, σ = global NLR magnitude standard deviation and Score = nondimensional sum of column ranks for $\bar{x}$,M, $G_\sigma^2 \times 10^3$, $\sum G$ and σ with a lower score representing higher overall statistical ranking within age category. Models denoted in bold italics discussed in the main text. Mean values for all models denoted in bold.

Table 5
Global Subduction Zone Kinematic Statistics Sorted by Trench Orthogonal Velocity Arithmetic Mean in Millimeters per Year

APM model	Age	$\lvert v\rvert\bar{x}$	$\lvert v\rvert M$	$\lvert v\rvert\ \sigma$	$\%_{ADV/RET}\ \bar{x}$	$\%_{ADV/RET}\ M$	Score
OptAPM5-M16	***80–0***	***22.79***	***16.17***	***22.8***	***0.32/0.68***	***0.32/0.68***	***6***
OptAPM9-M16	***80–0***	***22.89***	***16.2***	***22.87***	***0.33/0.67***	***0.32/0.68***	***9***
T2008	80–0	**23.71**	16.07	24.19	0.33/0.67	0.33/0.67	10
V2010	80–0	**23.92**	18.07	22.45	0.32/0.68	0.34/0.66	10
O2005	80–0	**25.4**	19.42	22.87	0.33/0.67	0.32/0.68	16
D2012	80–0	**26.61**	19.92	24.55	0.35/0.65	0.36/0.64	20
T2012	80–0	**28**	23.65	22.54	0.34/0.66	0.33/0.67	17
OptAPM1-M16	***80–0***	***28.82***	***16.95***	***38.33***	***0.32/0.68***	***0.32/0.68***	***20***
OptAPM5-M16	***120–0***	***24.01***	***17.28***	***26.08***	***0.31/0.69***	***0.33/0.67***	***6***
OptAPM9-M16	***120–0***	***24.19***	***17.52***	***25.95***	***0.31/0.69***	***0.33/0.67***	***8***
V2010	120–0	**25.24**	17.45	34.1	0.32/0.68	0.33/0.67	10
T2008	120–0	**27.75**	22.17	24.03	0.3/0.7	0.31/0.69	9
D2012	120–0	**28.99**	23.04	24.88	0.32/0.68	0.34/0.66	12
T2012	120–0	**31.65**	26.44	47.61	0.33/0.67	0.32/0.68	18
V2010	220–0	**25.92**	18.86	29.46	0.34/0.66	0.34/0.66	6
OptAPM5-M16	***220–0***	***27.23***	***16.16***	***45.22***	***0.34/0.66***	***0.34/0.66***	***8***
OptAPM9-M16	***220–0***	***27.46***	***16.37***	***44.96***	***0.34/0.66***	***0.34/0.66***	***9***
S2008	220–100	**27.66**	23.24	21.69	0.35/0.65	0.35/0.65	9
T2012	220–0	**28.92**	23.54	38.01	0.37/0.63	0.35/0.65	13

Note. APM model = absolute plate motion model, $\lvert v\rvert\bar{x}$ = global arithmetic mean absolute trench orthogonal velocity, $\lvert v\rvert M$= global median absolute trench orthogonal velocity, $\lvert v\rvert\sigma$ = global absolute trench orthogonal velocity standard deviation, $\%_{ADV/RET}\ \bar{x}$ = global arithmetic mean ratio of trench advance to retreat, $\%_{ADV/RET}\ M$ = global median ratio of trench advance to retreat, and *Score* = nondimensional sum of column ranks for $\lvert v\rvert\bar{x}$, $\lvert v\rvert M$, and $\lvert v\rvert\sigma$ with a lower score representing higher overall statistical ranking within age category. Models denoted in bold italics discussed in the main text. Mean values for all models denoted in bold.

APM models are generally similar, any discrepancies are assumed to be minimal. Each of the included published APM models in Figure 4 consistently produce approximately SW-NE "long-wavelength" motion for southern Africa with comparable magnitudes of rotation, however the "short-wavelength" motions show much greater disparity.

Table 6
Tally of Individual Model Assessment Metric Scores Sorted by Score Total

APM model	Age	RMS vel score	NLR score	TM score	Score total
OptAPM5-M16	**80–0**	**10**	**10**	**6**	**26**
OptAPM9-M16	**80–0**	**13**	**9**	**9**	**31**
OptAPM1-M16	**80–0**	**11**	**11**	**20**	**42**
T2008	80–0	21	18	10	49
T2012	80–0	29	31	10	70
V2010	80–0	24	30	17	71
O2005	80–0	35	30	16	81
D2012	80–0	34	27	20	81
OptAPM5-M16	**120–0**	**8**	**7**	**6**	**21**
OptAPM9-M16	**120–0**	**12**	**6**	**8**	**26**
T2008	120–0	18	17	9	44
V2010	120–0	21	24	10	55
T2012	120–0	17	25	18	60
D2012	120–0	28	24	12	64
OptAPM5-M16	**220–0**	**8**	**8**	**8**	**24**
OptAPM9-M16	**220–0**	**11**	**5**	**9**	**25**
S2008	220–0	19	16	9	44
V2010	220–0	14	22	13	49
T2012	220–0	23	22	6	51

Note. APM model = absolute plate motion model, RMS vel score, NLR score, and TM *score* = nondimensional sum of Score column ranks from RMS velocity, NLR rate, and trench migration metric assessment (Tables 3–5). Score total = sum of all nondimensional metric assessment scores with the lowest score representing the best overall statistical ranking and model performance within age category. APM models from this study are highlighted in bold. RMS vel = root-mean square velocity; NLR = net lithospheric rotation; TM = trench migration.

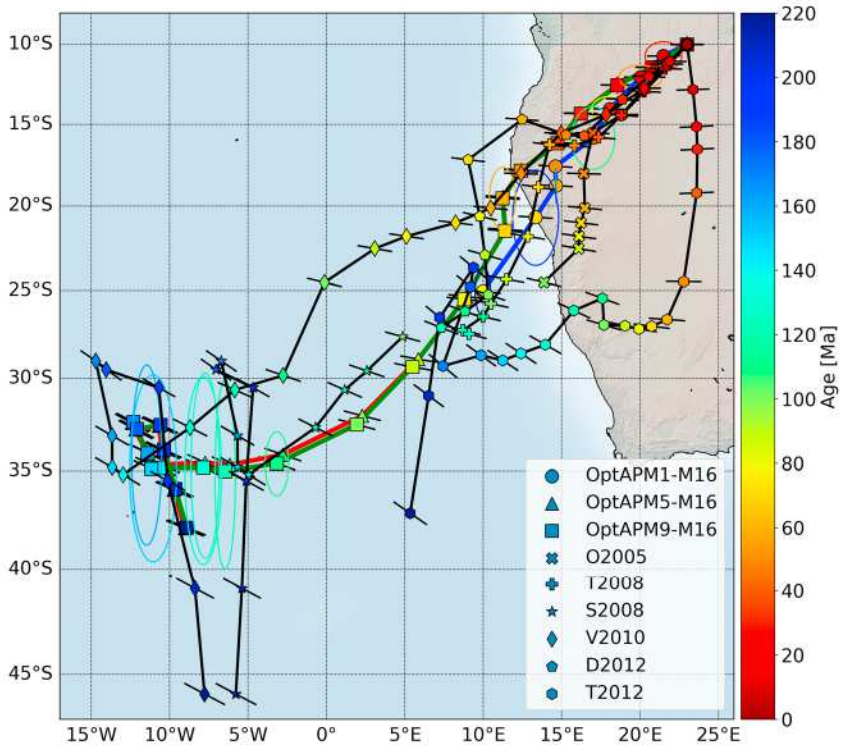

Figure 4. Predicted motion paths for a fixed point in southern Africa for selected absolute plate motion (APM) models. Models paths from this study OptAPM1-M16, OptAPM5-M16, and OptAPM9-M16 are colored blue, red and green respectively. Black lines represent the predicted motion paths of alternative published models: "X" symbols are O'Neill et al. (2005), "+" symbols are Torsvik, Müller, et al. (2008), star symbols are Steinberger and Torsvik (2008), diamond symbols are Van der Meer (2010), pentagon symbols are Doubrovine et al. (2012), and hexagon symbols are Torsvik et al. (2012). Symbol color represents age in million years, and distance between symbols represents distance covered in 10-Myr steps and direction of motion. Black horizontal lines on optimized paths represent the orientation of southern Africa relative to an E-W reference at 0 Ma. Ellipses color coded by age represent optimized model geographical uncertainties. Paths overlay ETOPO1 (Amante & Eakins, 2009).

The three hotspot-derived APM models from O'Neill et al. (2005), herein referred to as O2005, Torsvik, Steinberger, et al. (2008), herein referred to as T2008 and D2012 are evaluated, each applying an alternative approach and using a total of five individual hotspot tracks in their respective methods show similar behavior from ~50–0 Ma where hotspot data are more robust but diverge considerably for times ~130–50 Ma. The APM with the path representing the largest total motion of southern Africa, which in turn implies the highest plate velocities is the subduction history derived model taken from van der Meer et al. (2010), herein referred to as V2010. Although maintaining the general SW-NE motion, this APM model produces a path that is similar to the hotspot-derived paths for times younger than ~50 Ma but follows a much more northward trajectory between ~140 and 50 Ma creating a stronger west-to-east motion with a plate direction change at ~110 Ma. The smoothed TPW-corrected global apparent polar wander path (GAPWaP) derived from the APM model of T2012 generates a significantly different motion path to all other APM models for its entire duration of 220 Myr. The APM model is generated from an amalgamation of continental paleomagnetic data rotated into a fixed common reference frame (in this case South Africa) and combined into a single apparent polar wander path representing all paleomagnetic data globally. The combined GAPWaP is then smoothed via a running mean incorporating both the geographical uncertainty and the quality of the data to remove potentially anomalous rapid pole motions and cusps. Despite the running mean window used, the GAPWaP contains pronounced direction changes at ~110, ~100, and ~60 Ma, describing a very different motion path with less geographical displacement and a large deviation toward the southeast until ~60 Ma when the path moves almost directly northward to its present-day location. The final published reference frame shown in Figure 4 is the TPW corrected paleomagnetic data-derived reference frame for times older than 100 Ma of Steinberger and Torsvik (2008) herein referred to as S2008. Of all six alternative reference

frames discussed here, S2008 describes the smoothest path progression. As with V2010, the path at ~220 Ma is >45°S, producing a strong northward motion between ~220 and 190 Ma, before moving more gradually in a northeast direction.

In comparison to the published APM models, the three preferred APM models OptAPM1-M16, OptAPM5-M16, and OptAPM9-M16 produce significantly smoother reference plate motion paths, each with more uniformly spaced sample locations for their respective valid times through the entire period from ~150–0 Ma. Before 150 Ma, as a result of the breakup of Pangea (Müller et al., 2016; Seton et al., 2012; Shephard et al., 2013), the southern African path underwent rapid northward motion, followed by an anticlockwise motion while maintaining approximately the same azimuth. This motion is represented in each of the alternative APM models at varying degrees of magnitude, with the two optimized frames valid for this time producing the smallest magnitudes of motion of the cohort. The net effect of a smoother path with smaller-magnitude direction changes is minimized plate velocity acceleration and deceleration gradients, as well as minimizing global mean path velocities (shown in Figure 4), as the plate moves in a more direct and consistent manner within the same timeframe, which in the case of a plate reconstruction is considered a desirable property (Müller et al., 2016; Zahirovic et al., 2015).

5.1. Plate Velocities

RMS v_{rms} velocities were calculated for seven major continental blocks with a spatial sampling resolution of 1 degree using

$$v_{\text{rms}}=\sqrt{\frac{1}{n}\left(v_1^2+v_2^2+v_3^2+\ldots+v_n^2\right)} \tag{6}$$

where v_{rms} is the integrated RMS velocity of a given continental block, n is the total number of points used to sample the continental block, and v is the individual velocity calculated at each sample point. The accompanying table (Table 3) shows the summary statistical analyses of the calculated global RMS velocities for each APM model. For full model statistics of each continental block, see Table S2 in the supporting information. Continental RMS velocities are highly sensitive to the selected APM model coupled with a given RPM model, producing a wide range of velocities at a given age (Figure 5; Shephard et al., 2012). In all examples, continental velocity magnitudes are generally less than ~80 mm/Myr with a global average velocity calculated from all APM models in this study of ~34 mm/Myr, which is consistent with previous estimates of ~30 mm/Myr (Zahirovic et al., 2015). The only exception being India having the largest mean velocity of ~180 mm/Myr across all APM models, primarily due to its rapid northward motion toward Eurasia between ~70 and 50 Ma (Zahirovic et al., 2012).

A second feature of these examples is the identification of two key periods of maximum model velocity variation in all continental models. The first exists between ~220 and 160 Ma and shows a clear bimodal distribution of velocity profiles with APM models T2012, V2010, and S2008 displaying RMS velocities of almost double that of the optimized models, each on average ~30–50 mm/Myr faster. This anomalous velocity increase is a result of the predicted location of southern Africa at Pangea breakup in each APM model. T2012, V2010, and S2008 each position southern Africa further to the south (Figure 2), generating motion paths that are significantly longer than those constrained by the optimized models. As a direct result of this, southern Africa is required to move a greater distance within the same timeframe, with all three APM models introducing a pronounced northward motion during that time. The second period of variation exists between ~110 and 70 Ma is most likely caused by the specific choice of data used to constrain the APM models through this time. During this period, APM models using hotspot data become significantly more poorly constrained as few hotspot tracks remain. This is somewhat compounded as in both M16 and S13, the motion of the Pacific plate can no longer be linked to plates in the Indo-Atlantic realm via RPMs prior to ~83 Ma. This is also the period of introduction of paleomagnetic data as a APM model constraint, with "hybrid"-type models undergoing a transition from hotspot to paleomagnetic data at around ~100 Ma.

To more accurately compare continental velocities produced by each APM model, RMS velocity statistics were calculated independently for 80–0, 120–0, and 220–0 Ma, each incorporating all APM models valid for the respective time period (Table 3). For 80–0 Ma, OptAPM1-M16, OptAPM5-M16, and OptAPM9-M16 produce both the lowest mean and median global continental velocities of 31.9/26.3, 32/26.1, and 32.1/26.1 mm/Myr, respectively, each with a consistent global velocity gradient variance (GVGV) of 0.05.

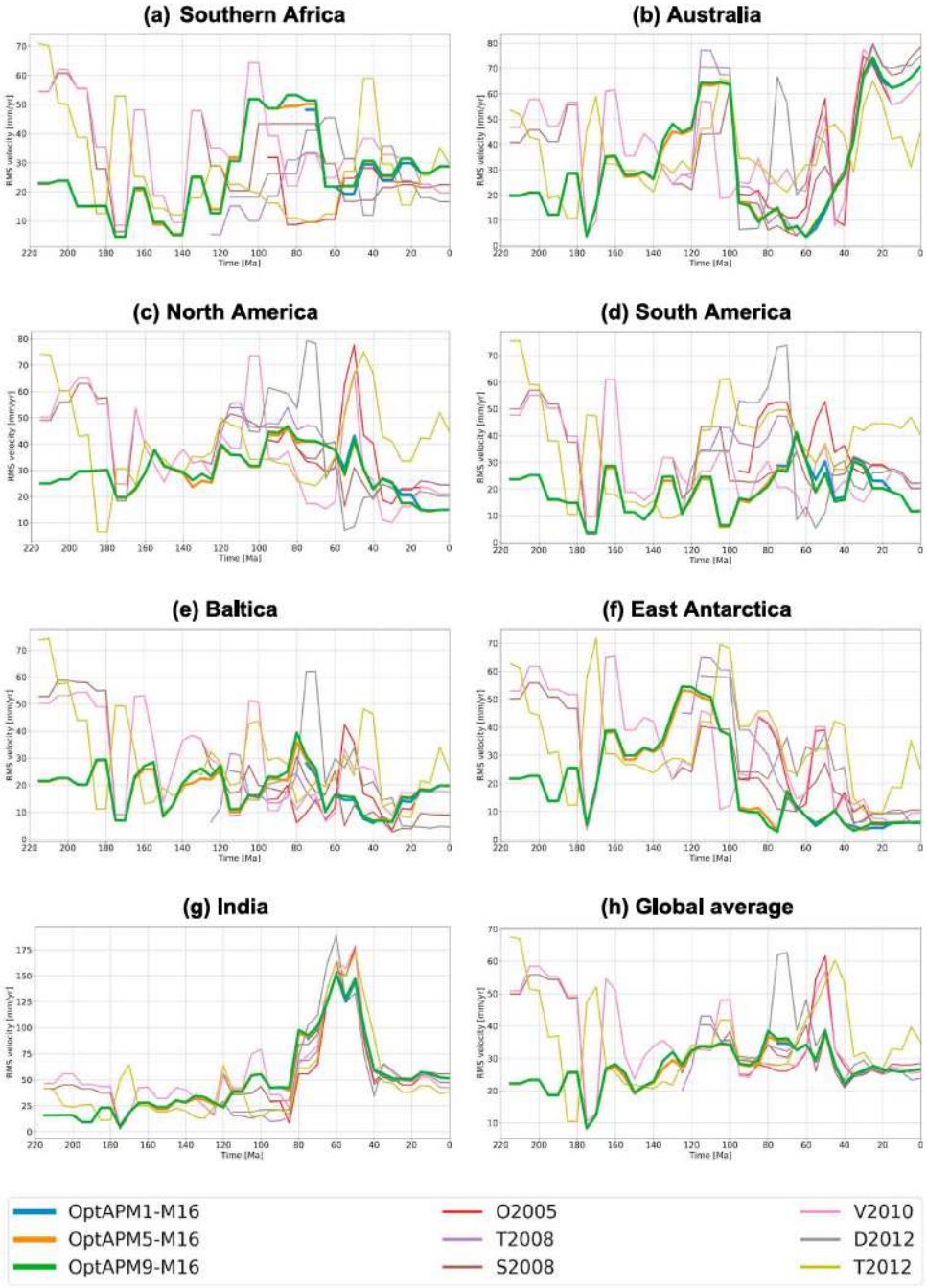

Figure 5. Root-mean square velocity v_{rms} plots for each optimized absolute plate motion (APM) and alternative published APM models with a spatial sampling of 1° and a temporal sampling of 1 Myr for seven major continental blocks: (a) southern Africa, (b) Australia, (c) North America, (d) South America, (e) Baltica, (f) East Antarctica, and (g) India, with (h) showing the calculated global mean root-mean square velocity for each APM model.

This statistic is the overall variance of the velocity gradients calculated at each time step, describing the fluctuation of global plate positive and negative acceleration magnitudes through time, with a lower value representing an APM that minimizes abrupt changes in continental velocities throughout the model period. The only published APM model for the period 80–0 Ma with a smaller GVGV is T2012 with 0.03. This result suggests T2012 minimizes plate accelerations very successfully when compared with the other APM models; however, it appears to do so at the expense of the global plate velocities themselves,

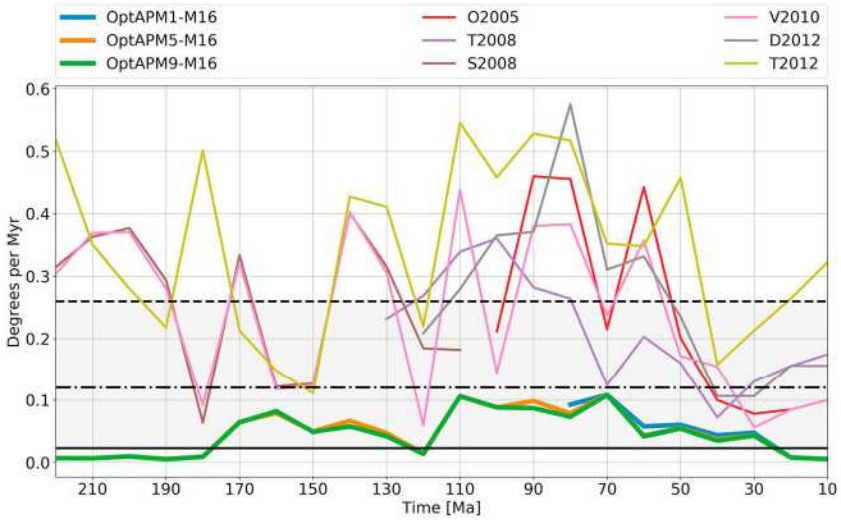

Figure 6. Comparison of net rotation magnitudes predicted by absolute plate motion (APM) models sampled at 2-Myr intervals and time averaged over 10-Myr intervals. Blue line is OptAPM1-M16, orange is OptAPM5-M16, green is OptAPM9-M16, red is O'Neill et al. (2005), purple is Torsvik, Müller, et al. (2008), brown is Steinberger and Torsvik (2008), pink is Van der Meer et al. (2010), gray is Doubrovine et al. (2012), and yellow is Torsvik et al. (2012). Black dashed horizontal line is the geodynamically defined present day net lithospheric rotation (NLR) upper limit of <0.26°/Myr taken from Conrad and Behn (2010). Black dash-dotted horizontal line is the estimated mean NLR of 0.12°/Myr for the past 150 Myr predicted in Torsvik et al. (2010). Black solid line represents estimated NLR lower limit of 0.023°/Myr from Becker (2006).

reporting the highest global arithmetic mean and median of all APM models of 40.5 and 36.3 mm/Myr, respectively (Table 3). The results for periods between 120–0 and 220–0 Ma are very similar, with the 120–0 Ma OptAPM5-M16 and OptAPM9-M16 models producing the smallest arithmetic mean and median velocities of 33/27.8 and 33.2/27.9 mm/Myr, both with a GVGV of 0.06, and in the 220–0 Ma category producing mean and median velocities of 28.7/25.7 and 29.1/26.3 mm/Myr with a respective GVGV of 0.11 and 0.1. Over the full 220–0-Ma time period, S2008 has mean velocities >7 mm/Myr faster and median velocities >6 mm/Myr faster. The 220–0 Ma GVGV also increases substantially from 0.09 at 120–0 Ma to 0.23 at 220–0 Ma suggesting much larger-magnitude plate motion changes during that period. As for the 80–0-Ma period, T2012 produced the lowest GVGV of 0.05 at 120–0 Ma while having the highest mean and median velocities of 39.2/35.6 mm/Myr. However, based on score, T2012 was the best performing published model overall for the full 220–0-Ma period, producing similar RMS velocity magnitudes to other models as well as the lowest GVGV of 0.08 for any model analyzed.

5.2. Net Lithospheric Rotation

Similar to RMS velocities, calculated NLR magnitudes show a wide range of values, again demonstrating the influence a given APM model has on a plate reconstruction (Figure 6). What is apparent from all APM models is that NLR appears to be a dynamic property of tectonics that is always in a state of flux. As a result of this, predicting only the mean or median NLR magnitude through time may not adequately describe all NLR behavior in given plate model as rates can fluctuate by more than 0.3 °/Myr (>60% of the total magnitude range of the models in this study have a value greater than the upper bound of <0.26°/Myr) over a single 10-Myr time step. As with the RMS velocity analysis, comparing NLR rate gradients and magnitudes provides greater insight into NLR behavior.

Of the published APM model rates of NLR (Table 4), T2008 produces the lowest NLR magnitudes and a global magnitude gradient variance (GMGV), a statistic like GVGV representing the fluctuation of global NLR magnitude positive and negative acceleration through time, with a lower value representing an APM that minimizes abrupt changes in rates of NLR from ~80–0 Ma and at ~130 Ma but exceeds the predicted upper bound from ~120–80 Ma. The model produces relatively smooth magnitude gradients from ~120–0 Ma, maintaining NLR rates between the estimated upper and lower bounds between ~80–0 Ma. S2008

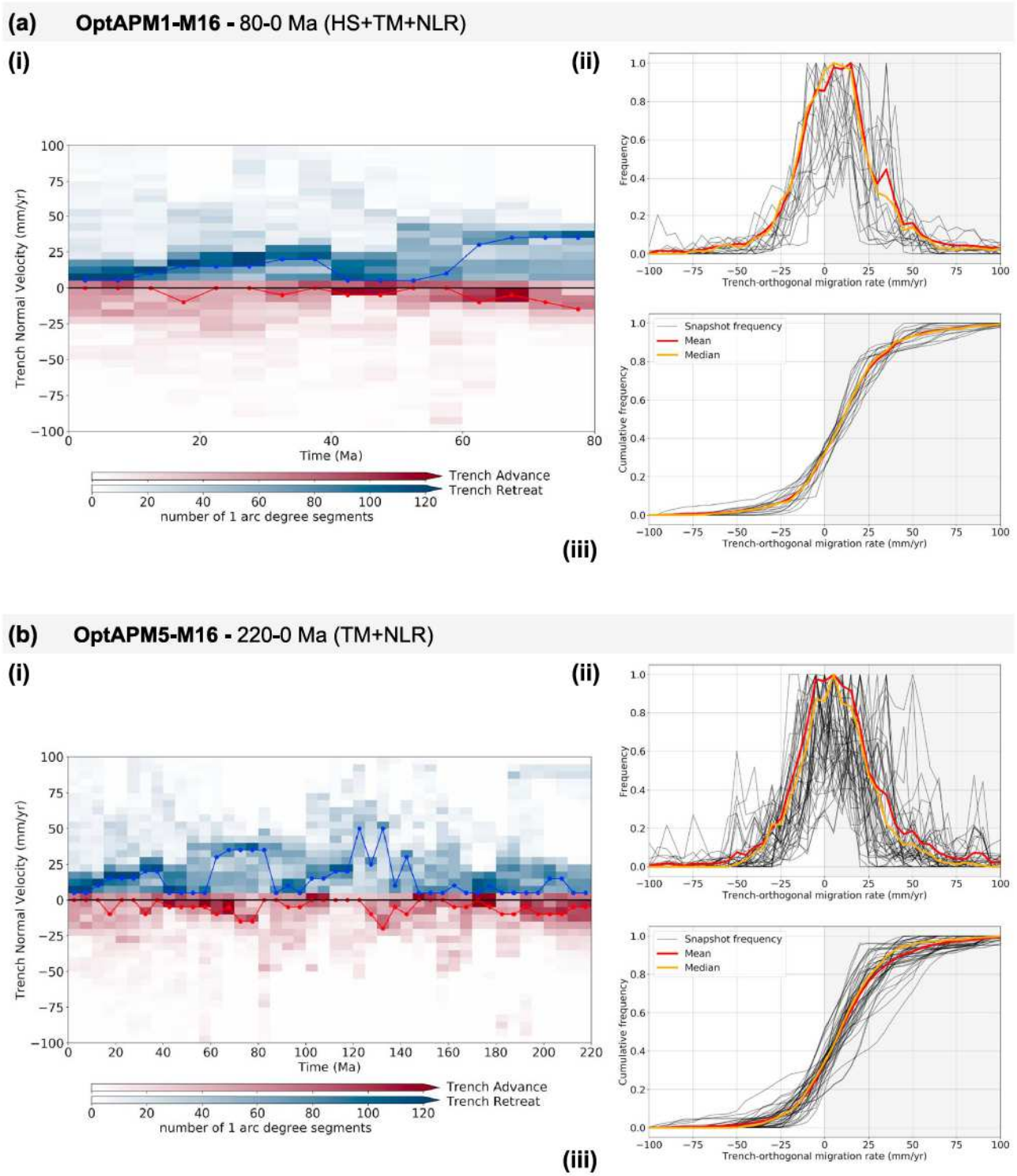

Figure 7. Subduction zone kinematics for each of the optimized absolute plate motion (APM) models OptAPM1-M16, OptAPM5-M16, and OptAPM9-M16 (a–c), and the two published models of O2005 and T2012 (d and e) representing the same periods. (i) Histograms representing rates of trench-orthogonal absolute motions through time with blue cells representing rates of trench retreat and red cells representing rates of trench advance. Solid blue and red lines represent histogram bin with highest-frequency trench normal retreat and advance velocity respectively. (ii) Trench motion frequency histograms with positive numbers representing rates of trench retreat and negative numbers representing rates of trench advance. (iii) Cumulative trench motion vectors and advance-to-retreat ratio with positive numbers representing rates of trench retreat and negative numbers representing rates of trench advance. Black lines represent model snapshots at 10-Myr increments. Red and orange lines represent cumulative motion mean and cumulative motion median, respectively.

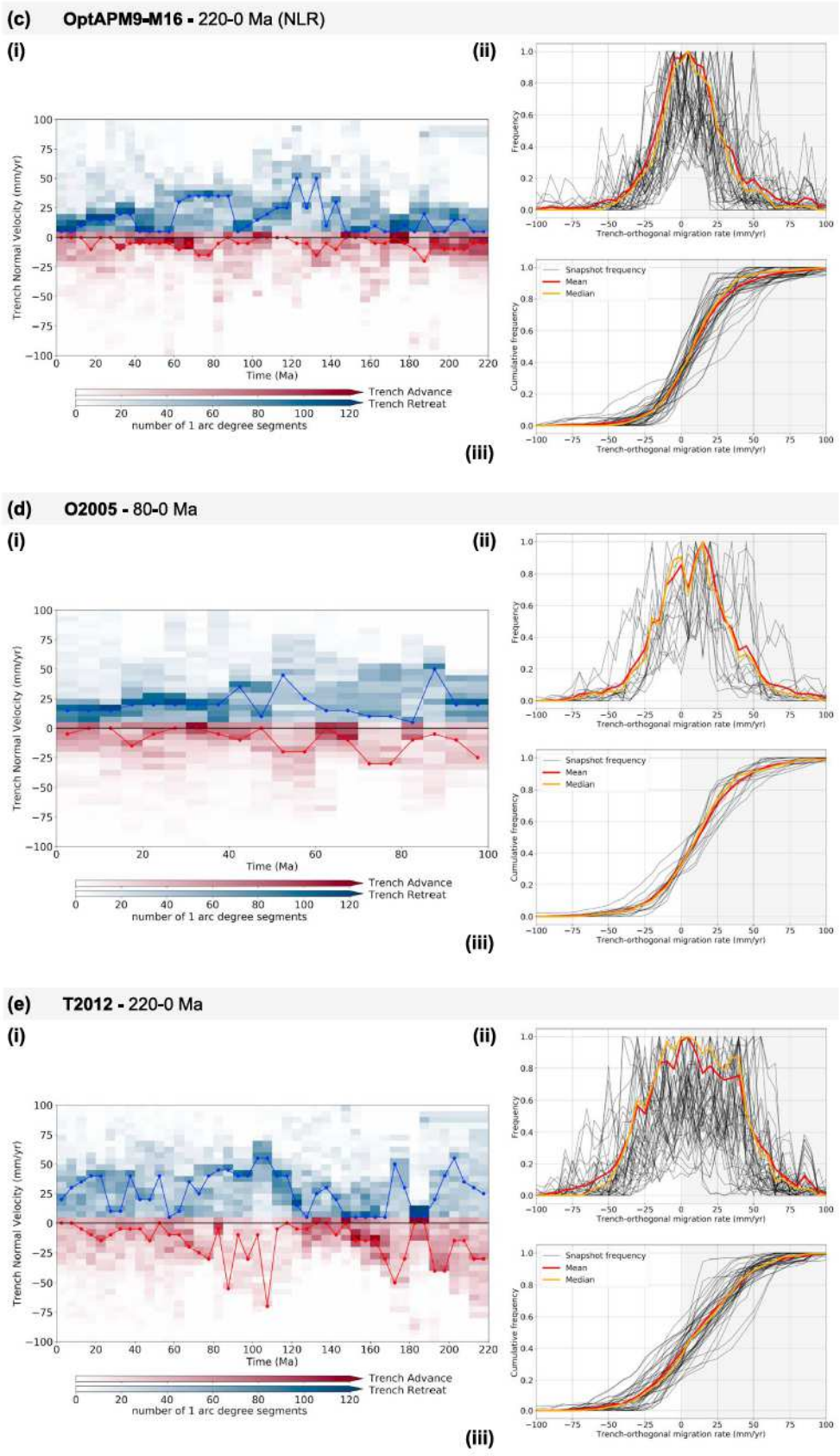

Figure 7. (continued)

produces the lowest arithmetic mean magnitude (°/Myr)/GMGVs of 0.206/0.606 for the period 220–0 Ma, but for times older than ~120 Ma, produces large NLR fluctuations that exceed the upper bound on seven occasions, the largest by ~0.14°/Myr. As described in the continental RMS velocity analysis, the calculated NLR magnitudes for each published model experience the same two prominent periods of maximum rate fluctuation at ~220–160 and ~110–70 Ma and is likely caused by the same model properties. In order to meet tectonic temporal and geographical constraints (based on the data used), models require larger plate velocities and in turn generate larger rates of NLR. Models O2005, V2010, and D2010 together display both large magnitudes and gradients of NLR prior to ~55 Ma, with O2005 producing the largest GMGV of any model between 80 and 0 Ma of 0.999. V2010 generates consistently large NLR gradients for all time steps, producing the maximum gradient of any model for both the 120–0- and 220–0-Ma periods of 0.996 and 1.303, respectively. D2012 produces the maximum NLR magnitude of any model of 0.575°/Myr at ~80 Ma, exceeding the estimated upper bound by 0.315°/Myr. The published model with the highest mean NLR magnitudes with high gradients throughout all analyzed periods is T2012. High rates of NLR are consistent with the findings of the continental RMS velocity analysis where T2012 produced large global plate velocities for all periods.

In contrast to each of the published models as the optimized APM models produced in this study include NLR minimization as a data constraint, models OptAPM1-M16, OptAPM5-M16, and OptAPM9-M16 all produce both the lowest NLR magnitudes and magnitude gradients. Each optimized model remains well beneath the estimated upper limit of 0.26°/Myr for all time steps, predicting highly minimized near-zero rates of NLR for times younger than ~25 Ma and times older than ~178 Ma, with arithmetic mean magnitudes that consistently remain within the 150-Myr mean of 0.12°/Myr from Torsvik et al. (2010), and the lower bound of 0.023°/Myr predicted by Becker (2006). As with the published models that incorporate hotspot data above, OptAPM1-M16 produces the greatest mean NLR magnitude 0.047°/Myr for 80–0 Ma.

5.3. Subduction Zone Kinematics

We compare a selection of subduction zone kinematic statistics to contrast the tectonic boundary behaviors predicted by the given APM models (Table 5). For the period 80–0 Ma, models OptAPM5-M16 and OptAPM9-M16 produced the least global subduction TM with mean/median absolute velocities of 22.8/16.2 and 22.9/16.2 mm/year, global absolute velocity standard deviations of 22.8 and 22.9 mm/year, respectively, with global mean and median trench advance to retreat ratios of 0.32:0.68 and 0.33:0.67/0.32:68, respectively, within published estimates of global trench advance to retreat ratios ranging between 0.38:0.62 and 0.22:0.78 (Schellart et al., 2008). Intuitively, these values can be interpreted as the given APM model producing an approximate trench advance to retreat ratio of 1:3 globally, while maintaining mean global absolute motion velocities of ~23 mm/year. For the period 80–0 Ma, OptAPM1-M16 produced the largest global mean absolute trench-orthogonal velocity of 28.8 mm/year, ~6 mm/year faster than optimal OptAPM5-M16 and is most likely a result of jointly fitting hotspot data with the other constraints, particularly hotspot data from the Pacific. Of the published models, T2008 and V2010 produced the smallest global mean/median absolute velocities of 23.7/16.1 and 23.9/18.1 mm/year, respectively. Moving back in time from 80 Ma, V2010 performs best of the published models for 120–0 Ma with mean/median trench-orthogonal velocities of 25.2/17.5 mm/year and produces the lowest global mean/median velocity values of 25.9/18.9 mm/year for the full 220–0-Ma period.

In comparing OptAPM1-M16 and O2005 (Figures 7a (i) and 7d (i)), each using hotspot data, both models produce stable global TM rates showing predominant retreat between ~30 and 0 Ma, with OptAPM1-M16 producing rate modes of ~15 mm/year or lower. However, prior to ~30 Ma, O2005 TM rates and gradients fluctuate with a peak mode retreat rate of ~55 mm/year at between 90 and 85 Ma and a trench advance rate peak of ~30 mm/year between 80 and 70 Ma. In contrast, back to 80 Ma OptAPM1-M16 produces more stable global trench motions, maintaining consistently low rates of trench advance of ~10–15 mm/year throughout the period with dominant trench retreat rates ranging from ~5 to a maximum of ~35 mm/year between 80 and 65 Ma producing higher mean but lower median rates than O2005 (Table 5.). This is also shown in the broader distribution of mean trench advance and retreat velocities for O2005 (Figures 7a (ii) and 7d (ii)), and greater dispersion of cumulative velocities in Figure 7a (iii) and 7d (iii). For the same time period, OptAPM5-M16 and OptAPM9-M16 produce similarly low rates of migration, each displaying rates of retreat/advance between 50 and 40 Ma of 0 and 5 mm/year, respectively. This is in contrast to T2012, which

suggests retreat rates of up to ~40 mm/year between 50 and 35 Ma, and advance rates of up to ~15 mm/year. Of the published models, V2010 consistently produces the lowest and most stable rates of trench retreat for 80–0 Ma, only fluctuating once between 55 and 50 Ma with a peak rate of ~50 mm/year but does show fluctuating rates of advance up to ~30 mm/year at 60–55 Ma. For times prior to 80 Ma, both OptAPM5-M16 and OptAPM9-M16 produce similar behaviors, with OptAPM9-M16 displaying a tighter clustering around the zero velocity line (Figure 7c (i)). Each of the optimal APM model histograms shows two main periods of rapid trench retreat at ~150–110 Ma and again at ~90–60 Ma. This result appears very similar to the shape of the NLR rate curves for the same models (Figure 6), indicating higher magnitudes of NLR are related to higher rates of TM, highlighting a potential, yet nonlinear, time-dependent correlation between these two components. However, the source of this apparent nonlinearity is not fully understood. Trench advance rates do not appear to correlate during these periods; however, OptAPM9-M16 generally produces lower rates of trench advance throughout.

In comparison with these models spanning 80–0 and 220–0 Ma, the paleomagnetic data derived T2012 model produce somewhat different trench behaviors that can be separated into three major TM events. The first, spanning ~220–160 Ma shows two major peaks in trench retreat at ~205 and ~170 Ma of up to ~55 mm/year with corresponding peaks in trench advance up to ~50 mm/year separated by a short period of slow trench retreat of ~5 mm/year and advance of ~20 mm/year between ~190 and 180 Ma that appears to coincide with the early onset of Pangea breakup. Similar migration fluctuations can be seen in OptAPM5-M16 at ~205 Ma and in OptAPM9-M16 at ~205 and ~190 Ma, however the velocities are 2–3 times smaller. The second event shows rates steadily increase from ~0 mm/year at ~135 Ma to a maximum of ~55 mm/year at ~110 Ma before returning to ~0 mm/year at ~60 Ma. During this same period, advance velocities show significant fluctuations up of up to ~70 mm/year at ~110 Ma, with the third period showing a rapid rise retreat rates since ~50 Ma (notably without a significant change in trench advance velocities) which again correlates with rising rates of NLR during this period. In comparing the migration rate distribution and cumulative statistics for each model (Figures 6a–6e (ii, iii)), the optimized models of OptAPM1-M16, OptAPM5-M16, and OptAPM9-M16 each show significantly tighter clustering around low velocities in the migration rate distribution plots, and less dispersion in the cumulative histograms. O2005 and T2012 each display generally broader retreat and advance rate distributions (highlighting larger migration rate variance), and greater cumulative rate dispersion.

Consistent with the findings of Williams et al. (2015), APM models minimizing TM predict APMs similar to those interpreted from subducted slab remnants interpreted from seismic tomography models in V2010. Most significantly as these predictions can be made without the need for the tomography model itself, providing subduction zones, including intraoceanic arc systems, are adequately represented in the RPM model (van der Meer et al., 2012, 2018).

5.4. Hotspot Motion and Trail Prediction

For recent times for which the present-day seafloor preserves a record of plate motions relative to hotspots via seamount chains, APM model quality can be directly tested by assessing the geographical fit of predicted hotspot tracks, in this case both against geological data and observed hotspot track geometry interpreted from marine gravity measurements (e.g., Andersen et al., 2010). Comparison of misfits for hotspot tracks from previously published APM models is complicated, as hotspot data-derived APM models are constrained using varying observations and contain different hotspot motion assumptions (unlike the metrics calculated for RMS velocities, NLR and TM behaviors in Tables 3–5). Assuming hotspot fixity, deviations between modeled and observed tracks indicate implied hotspot motion.

A series of predicted hotspot track cases from OptAPM1-M16, OptAPM5-M16, and OptAPM9-M16 were analyzed for the primary long-lived hotspots of Louisville, Hawaii, Réunion, and Tristan (Figure 8), with the mismatch between predicted observed track for the three APM models. Plots and estimated motion paths for the remaining hotspot tracks used in this study of Cobb, Foundation, St. Helena, Tasmantid, and Samoa derived using M16 and all hotspot tracks derived using S13 can be found in the supporting information. In the case of Louisville (Figure 8a), each of the modeled paths (shown as black lines) does successfully follow the same first-order geometry of the observed data points (stars), with OptAPM1-M16 (constrained by HS, TM, and NLR) producing the closest fit. However, each predicted path is seen to consistently appear shorter than observations and systematically plot eastward of the seamount chain. As these models were produced using a present-day location fixed hotspot assumption this mismatch is not unexpected but is relatively small

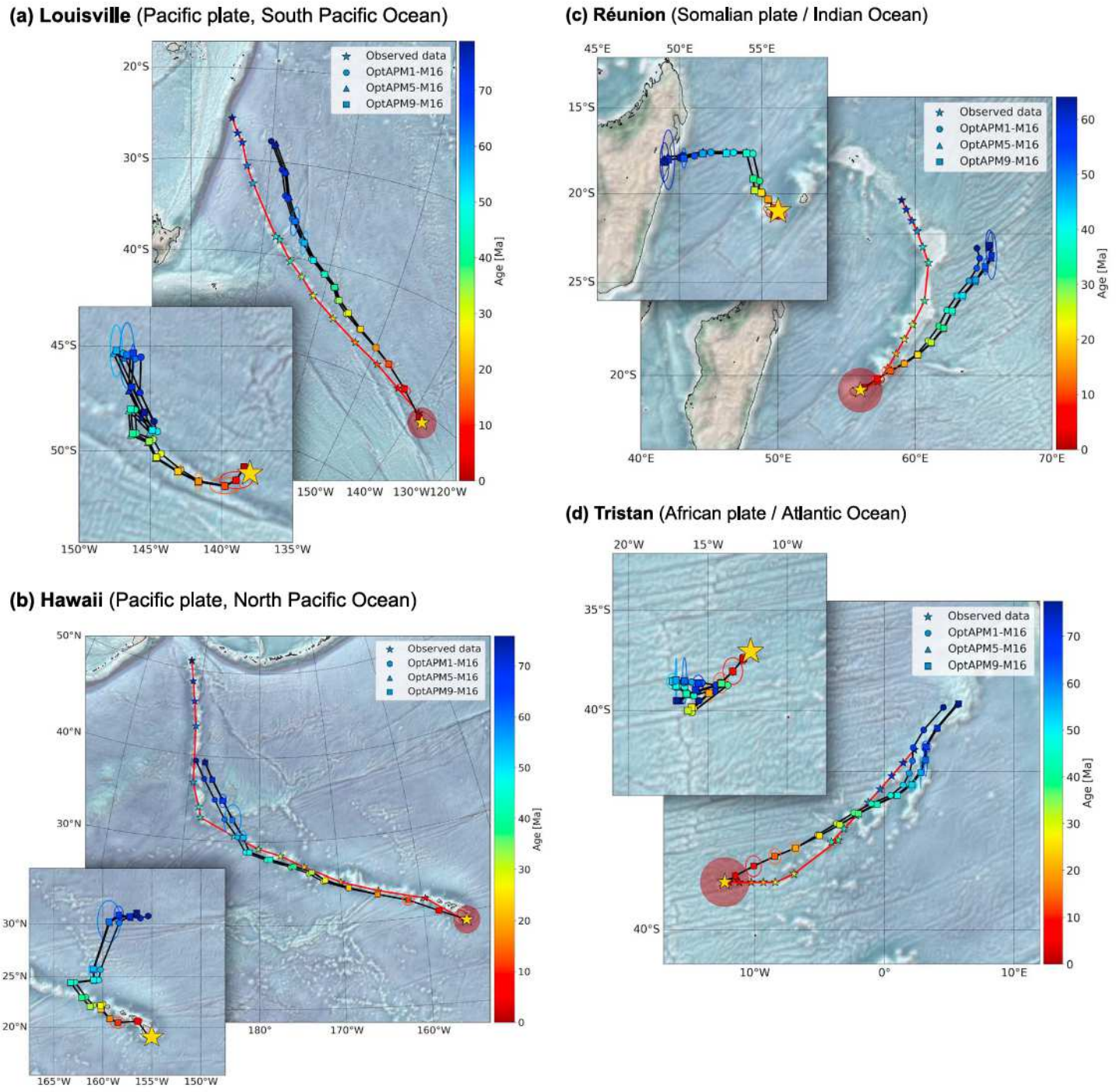

Figure 8. Predicted hotspot trails for absolute plate motion (APM) models OptAPM1-M16, OptAPM5-M16, and OptAPM9-M16 for (a) Louisville, (b) Hawaii, (c) Réunion, and (d) Tristan. Inset: Estimated independent hotspot motion paths derived from fixed-hotspot track prediction and interpolated volcanic observations misfit. Ellipses are color coded by observation age and represent calculated model geographic uncertainties. Red line marks the resulting hotspot track when the fixed-hotspot trail prediction is corrected using the estimated hotspot motion model. Stars represent interpolated seafloor volcanic observations. Large gold star is estimated present-day location of hotspot. Red circle represents approximate present-day hotspot locations with an estimated 2° uncertainty ellipse. Paths overlay ETOPO1 (Amante & Eakins, 2009) and global marine gravity (Andersen et al., 2010). Motion path values for all hotspots used in this study are listed in Table S3 in the supporting information.

considering geological observations and mantle flow modeling provide strong evidence to suggest global hotspots move relative to one another (Divenere & Kent, 1999; Hassan et al., 2016; Koppers et al., 2004; *Koppers* et al., 2011; Koppers et al., 2012; Molnar & Atwater, 1973; Molnar & Stock, 1987; Tarduno et al., 2003). Perhaps, the most significant result of this study is the demonstrated ability of global APM models derived without explicit hotspot data constraint to produce plate reconstructions that predict both hotspot chain geometries and independent hotspot motions that are consistent with observations (Figure 8). In particular, the fact that APM models constrained solely through the minimization of global NLR or TM fit seafloor observations, themselves quantities independent of any hotspot trail data, presents the opportunity to derive APM models for deep time when geological observations such as hotspot trails are no longer available.

The misfit between the predicted and the observed chains can be interpreted as approximating the motions of the associated hotspot, with the combined fixed hotspot predicted track and associated predicted hotspot motion path plotted as the red line. For Louisville (Figure 8a and Table 7), the estimated mean rate of hotspot motion is ~21 mm/Myr, with a maximum rate of ~84 mm/Myr during a unique rapid southeastward motion of ~4° between ~55 and 50 Ma, consistent with previous estimates of Louisville motion based on paleomagnetic and geochronological analyses that suggest the hotspot has remained within 3–5° of its present-day latitude between ~70 and 50 Ma (Koppers et al., 2004; Koppers et al., 2012). Each APM model also predicts an approximate longitudinal motion of ~3–5° between ~78–30 Ma, which again is consistent with previous estimates of ~5° between 80 and 30 Ma (Koppers et al., 2011). A similar style of systematic misfit is observed for the Hawaiian portion of the Hawaiian-Emperor chain (Figure 8b), with the predicted track consistently plotting slightly southward of the observed seamount chain, and like Louisville, not reaching the full length of the observed seamount chain creating an geographically "offset" bend at ~50 Ma. The associated estimated mean rate of hotspot motion (Figure 8b and Table 7) for Hawaii is ~24.1 mm/Myr, with a maximum rate of ~92.8 mm/Myr between ~60 and 55 Ma during a rapid southwestward latitudinal motion of ~5°, followed by a second burst between ~50 and 45 Ma of ~48.8 mm/Myr associated with a rapid westward motion of ~2–3°. The identification of a rapid latitudinal motion appears consistent with previous observational estimates from paleomagnetic data of 11–15° between 81 and 47 Ma (Tarduno et al., 2003; Tarduno et al., 2009), and a more recent study that estimated ~7° of rapid differential motion between the Hawaiian and Louisville hotspots over a 22-Myr period between 60 and 48 Ma by comparing their time-dependent spatial relationship with the newly mapped Rurutu hotspot track on the Pacific plate (Konrad et al., 2018). Analysis of poloidal flow under the Pacific plate since 100 Ma driven by the oceanward migration of subduction zones in the northern Pacific produce congruent estimates of Hawaiian hotspot motion, predicting ~10° of southward latitudinal motion between 81 and 47 Ma (Hassan et al., 2016; Steinberger, 2000; Steinberger et al., 2004). This result is consistent with both observational estimates and the APM model predictions from this study, providing a potential physical driving mechanism for the observed rapid motion of the Hawaiian plume. However, the model of Hassan et al. (2016) does not appear to predict the motion of Louisville during the same period.

The Réunion hotspot and associated trail have received little attention (O'Neill et al., 2003). Evidence for motion of Réunion primarily comes from a data set of only three paleolatitude estimates derived from the paleomagnetic study of unoriented basalt and sediment drill core taken from Ocean Drilling Program Leg 115 drill sites 706 (~35.8 Ma sediment), 707 (~63.9 Ma basalt), and 715 (~57.5 Ma basalt), which when combined report an estimated northward drift of Réunion of 8 mm/year between 67 Ma and present day (Vandamme & Courtillot, 1990; Schneider & Kent, 1990). However, due to the limited nature of paleomagnetic analysis available using ocean core, when the data are evaluated using the paleomagnetic data quality criteria, samples average a relatively low Van der Voo (1990) *Q* score of 3 (out of a possible 7), as (i) the number of sample sites used per result (*N*) is less than 24 (706, 715), (ii) A95 uncertainties fluctuate up to a maximum 20° (707), true field tests are not possible (a single positive quasi-fold test is reported for the site 706 sediments), (iii) structural controls remain unknown (all basement samples are assumed horizontal), (iv) reversals cannot be detected as core is not oriented, and (v) as paleomagnetic poles are not being calculated, no comparison can be made against poles of younger age to confirm magnetization is primary. In addition, application of methods to detect and correct for possible inclination shallowing in the sediments (site 706) is not reported, and it is suspected secular variation is not averaged for site 707 (Vandamme & Courtillot, 1990; O'Neill et al., 2003). Based on these uncertainties, the prediction of a definable ~5° of northward motion for the Réunion hotspot between ~64 and 36 Ma from Ocean Drilling Program Leg 115 data is not possible as the

Table 7
Estimated Independent Absolute Motion Paths of Hotspots Using OptAPM1-M16

Hotspot trail	Latitude (°)	Longitude (°)	Period (Ma)	Velocity (mm/Myr)
Louisville	−51.0	−138.0	0	—
	−50.7	−138.4	7–0	12.7
	−51.3	−139.0	13–7	10.0
	−51.6	−139.8	18–13	25.4
	−51.3	−141.6	24–18	19.0
	−50.8	−142.9	30–24	22.2
	−50.1	−144.2	35–30	15.8
	−49.5	−144.8	40–35	16.1
	−49.2	−146.0	46–40	24.0
	−48.1	−146.1	51–46	29.9
	−49.1	**−144.5**	**56–51**	**82.6**
	−45.4	−146.9	62–56	12.5
	−45.6	−146.1	68–62	5.7
	−45.5	−145.7	73–68	36.3
	−47.2	−145.7	79–73	30.0
Hotspot trail	Latitude (°)	Longitude (°)	Period (Ma)	Velocity (mm/Myr)
Hawaii	19.0	−155.0	0	—
	20.6	−156.4	5–0	45.1
	20.5	−158.5	11–5	36.4
	20.9	−159.3	17–11	16.5
	21.9	−160.1	22–17	24.9
	22.3	−160.0	28–22	10.0
	22.2	−160.9	33–28	19.9
	23.0	−161.7	38–33	24.5
	24.5	−162.8	43–38	34.0
	24.7	**−160.4**	**48–43**	**48.8**
	25.7	−160.2	54–48	19.6
	30.1	**−158.3**	**60–54**	**92.6**
	30.7	−157.3	66–60	19.5
	30.6	−156.2	71–66	22.6
	30.8	−155.4	76–71	15.9
Hotspot trail	Latitude (°)	Longitude (°)	Period (Ma)	Velocity (mm/Myr)
Réunion	−21.0	56.0	0	—
	−21.2	55.8	6–0	4.8
	−21.2	56.0	12–6	9.6
	−20.8	55.8	16–12	13.4
	−20.4	55.4	22–16	10.7
	−20.0	55.0	26–22	5.3
	−19.9	54.8	32–26	13.4
	−19.3	54.9	38–32	32.2
	−17.7	54.5	42–38	25.0
	−17.6	53.3	48–42	29.3
	−17.6	51.9	53–48	19.3
	−17.8	50.9	59–53	12.5
	−17.8	50.2	64–59	4.7
Hotspot trail	Latitude (°)	Longitude (°)	Period (Ma)	Velocity (mm/Myr)
Tristan	−37.1	−12.3	0	—
	−37.5	−12.8	8–0	17.7
	−38.1	−13.4	14–8	15.5
	−38.7	−14.2	20–14	14.2
	−39.2	−15.0	26–20	19.4
	−40.0	−15.9	31–26	4.5
	−40.0	−16.0	37–31	40.6
	−38.8	−13.8	42–37	37.0
	−39.3	−15.9	48–42	13.5
	−38.9	−16.5	52–48	5.2
	−38.6	−16.5	58–52	8.3
	−38.6	−16.0	62–58	11.7

Table 7
(continued)

Hotspot trail	Latitude (°)	Longitude (°)	Period (Ma)	Velocity (mm/Myr)
	−38.7	−15.4	68–62	15.5
	−38.8	−14.5	72–68	6.8
	−39.1	−14.6	78–72	20.4

Note. Latitude = estimated motion path paleolatitudes, Longitude = estimated motion path paleolongitudes, Period = approximate period for each path motion velocity calculation, *Velocity* = estimated hotspot path segment velocity in millimeters per million years. Values highlighted in bold represent periods of anomalous hotspot motion and are described in the main text. Estimated independent absolute hotspot motions for all hotspots used in this study for both M16 and S13 can be found in Table S3 the supporting information.

magnitude of the latitudinal uncertainty is greater than the prediction, but does however provide some observational guidelines as to the broad latitudinal behaviors of the Réunion hotspot during this period. The resulting models of Réunion motion from this study (Figure 8c and Table 7) describe a somewhat different hotspot evolution to that predicted by the above studies (Vandamme & Courtillot, 1990; Schneider & Kent, 1990), however, remain consistent with the identified paleomagnetic latitudinal uncertainty bounds and shares characteristic eastward migration features with geodynamic models of surface hotspot motions (O'Neill et al., 2003; Steinberger, 2000; Steinberger & O'Connell, 1998). The initial period of eastward motion between ~65 and 45 Ma at a near constant latitude of ~17.7° is consistent with the latitude of site 707 at ~64 Ma of −25.2° ± 10°, the latitude of site 715 at ~57.5 Ma of −25° ± 5.8°, and interestingly also with the latitude of site 713 at ~47.5 Ma of −12.3° ± 3.1°, which was excluded from the Réunion model of Vandamme and Courtillot (1990) as it was considered anomalous. The subsequent southeastward motion of the Réunion model in this study between ~38 Ma and present day does correlate with a predicted hotspot latitude of −19.6° falling at the upper bound of the observed latitudinal uncertainty of site 706 at ~35.8 Ma of −12.7° ± 6.9°. The predicted longitudinal motion of Réunion in this study of ~6° remains unconstrained by the paleomagnetic data but is very similar to the magnitude of longitudinal motion of ~8° predicted in mantle flow models (O'Neill et al., 2003; Steinberger, 2000; Steinberger & O'Connell, 1998).

The Tristan hotspot (Figure 8d and Table 7) shows quite different behavior to Hawaii, Louisville, and Réunion. Each of the predicted paths fit the observed geometry generally well, producing track progressions slightly longer than the observed data would suggest. Unlike the Pacific chains, the predicted Tristan chains change from plotting consistently southward of observations between ~80 and 45 Ma, to consistently plotting northward of observations from ~45–0 Ma. The predicted hotspot motion path does not suggest the Tristan hotspot has moved any significant distance over the past ~80 million years, with an apparent plume "wobble" of only approximately 2–3° that is within calculated model uncertainty ellipses (Figure 8d and Table 7), which represent the spatial distribution of given hotspot locations from all models.

It would appear based on the results of this study in addition to the consistent results of these published multidisciplinary analyses that the observed geometries and age progressions of hotspot trails are the net expression of multiple factors. To move toward the calculation of accurate fits to global hotspot track data, models need to incorporate the combined influence of APMs, RPMs derived from geologically sound plate circuits, and hotspot motions that are consistent with geological observations (Matthews et al., 2015).

5.5. Applicability, Considerations, and Future Outlook

The optimization method presented provides a practical and efficient workflow for deriving APM models, requiring only a topological or "full plate" reconstruction (e.g., Seton et al., 2012; Domeier & Torsvik, 2014; Müller et al., 2016, 2019; Merdith et al., 2017). The primary advantage of this approach is that it does not necessarily require any additional data sets (such as hotspot trail data), though these can be included where available. Therefore, the method has the potential to be applied to derive APM models for pre-Triassic times, the period of Earth's history that cannot be constrained by hotspot trails, which are limited by the preservation of post-Pangea oceanic crust (Müller et al., 2016; Seton et al., 2012), or by current approaches to mapping slab remnants modeled by seismic tomography (Boschman & van Hinsbergen, 2016; Domeier et al., 2017; van der Meer et al., 2012). Additionally, the method can jointly evaluate multiple constraints, permitting investigations of potential correlations that may exist between individual

components, better assessment of the risk of bias where fits are calculated from only one type of data, and inform the relative weighting of system components such as NLR and TM. This is of particular importance when integrating hotspot trail data as observations are not evenly distributed among plates (e.g., plates with many trails such as the Pacific or African compared to plates with relatively few trails such as North American or Eurasian (McDougall & Duncan, 1988; O'Neill et al., 2005; Knesel et al., 2008; Wessel & Kroenke, 2008; Doubrovine et al., 2012; Koppers et al., 2012; O'Connor et al., 2013). APM models derived using this joint approach incorporating the more globally uniform geographic distributions of plate and trench kinematics have quantitatively smoother plate motions compared with many previous APM models derived from fitting hotspot trails alone (Figure 4).

The incorporation and exploration of applying NLR as a direct constraint on plate reconstruction model behavior requires a complete and self-consistent representation of plate configurations at all time steps (*Gurnis* et al., 2012), with configurations becoming increasingly uncertain back through time with a proportional increase in the estimated "world uncertainty" relative to the loss of preserved seafloor (Müller et al., 2016; Torsvik et al., 2010; Torsvik & Cocks, 2016). This uncertainty present in RPM models is most apparent in models of oceanic regions for times older than 160 Ma, where to remain self-consistent, reconstructions require the inclusion of synthetic plates to describe regions that have since been subducted (e.g., Panthalassa) and cannot be directly observed. As a result, synthetic boundaries are also required, again increasing the uncertainty of plate geometries and subsequent velocity calculations (Müller et al., 2016; Seton et al., 2012). A second consideration is identifying the range of acceptable NLR rotation magnitudes to be applied in a given optimization. For this study an assumption that NLR must be small but nonzero is applied based on published geodynamic estimates. However, as this is primarily a theoretical quantity, this range remains to be further explored in future work. For Paleozoic and older times, increasing levels of plate boundary uncertainty (both geometry and location) also has ramifications for the use of TM rates as a deep time constraint (Merdith et al., 2017; Tetley et al., 2019). Addressing these uncertainties in plate models is a difficult task, as uncertainty is typically a function of available data and therefore reconstruction age. A next step in this process could be in the integration of deep time data sets not considered here as a constraint, such as paleomagnetic data, although this would potentially introduce additional complications such as identifying, quantifying, and integrating estimates of TPW directly either through the application of existing methods (and associated assumptions), or through the development of new methods. This would provide an independent "platform" from which time-dependent APM model steps can be evaluated similar to the approach of sequential data assimilation methods (*Bocher* et al., 2016). It is also important to keep in mind that APMs resulting from the method presented here are sensitive to the choice of relative weighting of each integrated constraint. These weights are not known a priori, and while beyond the scope of this study, further exploration of these parameter choice would be valuable.

APM models derived using RPM models in the method presented in this manuscript are a direct function of the specific plate reconstruction model used, both in terms of the relative rotations and the topological plate geometries, making them highly sensitive to plate reconstruction model predictions. Consequently, it is not strictly appropriate to arbitrarily apply the resulting plate motion parameters derived from one reconstruction to another as they are incompatible due to this dependency. Instead, independent APM models should be recalculated for alternative plate models, or, as existing models are modified including the plate geometries, plate configurations, relative relationships between adjacent plates, subduction trench location and geometry, or the applied plate circuit model. The influence of relative plate motion model (RPM) choice is revealed by our results for the model of Shephard et al. (2013) in the supporting information (Table S1 and Figures S1 and S2), compared to the model of Müller et al. (2016) discussed in the main text. This is most clearly demonstrated by comparing hotspot track fits, in particular, the ability for a given APM/RPM combination to predict the bend in the Hawaiian-Emperor track (Figure S1). The differences between APM results produced using different histories of RPMs and plate boundary evolution show that APM models derived using this method are highly dependent and sensitive to the plate reconstruction (RPM) used, such as the time-dependent geometries and locations of plate boundaries, the selected plate circuit (as described in section 3) and the quality of both input data and associated interpretation. This is of greatest importance when deriving APM models further back in time as RPM uncertainty significantly increases with the loss seafloor data. As demonstrated in this study, although optimized APM models have the ability to improve the global first-order geodynamic characteristics of a given RPM via identifying best fitting solutions, they

do not have the ability to modify the RPM, further emphasizing the need to recognize and quantify plate reconstruction uncertainty. This provides an additional motivation to further improve topological reconstructions themselves, in addition to investigating the how plates and plate boundaries have moved relative to the mantle.

6. Conclusions

The derivation of APM models consistent with global geological observations and first-order geodynamic principles is crucial to the development of modern, full plate tectonic reconstructions. A key element is the recognition of the need to jointly incorporate multiple constraints into global model development to derive and evaluate APM model behavior through time. Through the simultaneous use of multiple constraints, APM models are less likely to suffer from overfitting a single constraining quantity such as hotspot track or paleomagnetic data (i.e., often at the cost of large misfit with other observations) and produce global plate velocities and velocity gradients consistent with geodynamic estimates. Additionally, the direct integration of first-order geodynamic principles as constraints alongside observations provides a practical method to increase the geodynamic consistency of global plate reconstructions. Global APM models derived using this method demonstrate global fit to geological observations while quantitatively optimizing desirable first-order geodynamic behaviors which are not necessarily explicitly encoded within RPM models. Significantly, this study demonstrates an ability for APM models to be constrained solely by using the geodynamic principles of NLR (220–0-Ma average of ~0.05°/Myr) and TM (220–0-Ma absolute average of ~27 mm/year). These models, derived without explicit constraint from observations, successfully produce global plate reconstructions accordant with (1) observed hotspot trail geometries and age progressions, (2) independent hotspot motions consistent with published observations and geodynamic experiments, and (3) desirable global plate velocity behaviors. This result highlights not only the relative influence and magnitude of these geodynamic quantities within the tectonic system for the past 220 Ma but more broadly the importance of considering and explicitly applying our geodynamic understanding of the Earth into the development of plate reconstructions. Of particular potential is the application of this geodynamically informed workflow to constrain deep time plate and continental motions where observations are limited, potentially providing more robust tectonic predictions for communities who routinely utilize plate reconstructions as a constraint for geodynamics, ocean circulation, or climate modeling.

Acknowledgments

This research was supported by the Science Industry Endowment Fund (RP 04-174) Big Data Knowledge Discovery Project together with Australian Research Council Grants IH130200012 and DE160101020. M. G. T. received additional support from a CSIRO-Data 61 Postgraduate Scholarship. M. G. was supported by the National Science Foundation (EAR-1645775). The authors would like the thank the two anonymous reviewers for their careful and constructive comments that served to improve the paper, together with Sabin Zahirovic and John Cannon for their combined technical help and expertise to make this research possible. This is a contribution to IGCP project 648. Analyses were conducted using the following open source tools: GPlates and pyGPlates (www.gplates.org), Python (www.python.org), and Project Jupyter (www.jupyter.org). The digital files associated with this analysis and for the plate reconstruction using the GPlates software are archived online (doi:10.5281/zenodo.2638121).

References

Amante, C. and B.W. Eakins (2009), ETOPO1 1 arc-minute global relief model: Procedures, data sources and analysis. NOAA Technical Memorandum NESDIS NGDC-24. National Geophysical Data Center, NOAA. doi:https://doi.org/10.7289/V5C8276M [Accessed 10 May, 2016]

Andersen, O. B., Knudsen, P., & Berry, P. (2010). The DNSC08GRA global marine gravity field from double retracked satellite altimetry. *Journal of Geodesy*, *84*(3), 191–199. https://doi.org/10.1007/s00190-009-0355-9

Argus, D. F., & Heflin, M. B. (1995). Plate motion and crustal deformation estimated with geodetic data from the Global Positioning System. *Geophysical Research Letters*, *22*(15), 1973–1976. https://doi.org/10.1029/95GL02006

Becker, T. W. (2006). On the effect of temperature and strain-rate dependent viscosity on global mantle flow, net rotation, and plate-driving forces. *Geophysical Journal International*, *167*(2), 943–957. https://doi.org/10.1111/j.1365-246X.2006.03172.x

Becker, T. W., & Faccenna, C. (2011). Mantle conveyor beneath the Tethyan collisional belt. *Earth and Planetary Science Letters*, *310*(3–4), 453–461. https://doi.org/10.1016/j.epsl.2011.08.021

Becker, T. W., Schaeffer, A. J., Lebedev, S., & Conrad, C. P. (2015). Toward a generalized plate motion reference frame. *Geophysical Research Letters*, *42*, 3188–3196. https://doi.org/10.1002/2015GL063695

Bocher, M., Coltice, N., Fournier, A., & Tackley, P. J. (2016). *A sequential data assimilation approach for the joint reconstruction of mantle convection and surface tectonics*, *Geophysical Journal International*, (Vol. 204, pp. 200–214). Oxford University Press. https://doi.org/10.1093/gji/ggv427

Boschman, L. M., & van Hinsbergen, D. J. J. (2016). On the enigmatic birth of the Pacific Plate within the Panthalassa Ocean. *Science Advances*, *2*(7). https://doi.org/10.1126/sciadv.1600022

Boyden, J. A., Muller, R. D., Gurnis, M., Torsvik, T. H., Clark, J. A., Turner, M., et al. (2011). Next-generation plate-tectonic reconstructions using GPlates. In G. R. Keller, & C. Baru (Eds.), *Geoinformatics: Cyberinfrastructure for the Solid Earth Sciences*, (pp. 95–113). Cambridge: Cambridge University Press. https://doi.org/10.1017/CBO9780511976308.008

Burke, K., Steinberger, B., Torsvik, T. H., & Smethurst, M. A. (2008). Plume generation zones at the margins of Large Low Shear Velocity Provinces on the core–mantle boundary. *Earth and Planetary Science Letters*, *265*(1-2), 49–60. https://doi.org/10.1016/j.epsl.2007.09.042

Butler, R. F. (1991). *Paleomagnetism: Magnetic domains to geologic terranes*. Blackwell Science.

Conrad, C. P., & Behn, M. D. (2010). Constraints on lithosphere net rotation and asthenospheric viscosity from global mantle flow models and seismic anisotropy. *Geochemistry, Geophysics, Geosystems*, *11*, Q05W05. https://doi.org/10.1029/2009GC002970

Cuffaro, M., Doglioni, C., & Università, S. (2007). Global kinematics in deep versus shallow hotspot reference frames. *Society*, *430*(18), 359–374. https://doi.org/10.1130/2007.2430(18)

DeMets, C., Gordon, R. G. and Argus, D. F. (2010) *Geologically current plate motions*, *Geophysical Journal International*. Oxford University Press, 181(1), pp. 1–80. https://doi.org/10.1111/j.1365-246X.2009.04491.x.

Deschamps, F., & Tackley, P. J. (2008). Searching for models of thermo-chemical convection that explain probabilistic tomography: I. Principles and influence of rheological parameters. *Physics of the Earth and Planetary Interiors*, *171*(1-4), 357–373. https://doi.org/10.1016/j.pepi.2008.04.016

Deschamps, F., & Tackley, P. J. (2009). Searching for models of thermo-chemical convection that explain probabilistic tomography. II—Influence of physical and compositional parameters. *Physics of the Earth and Planetary Interiors*, *176*(1–2), 1–18. https://doi.org/10.1016/j.pepi.2009.03.012

Divenere, V., & Kent, D. V. (1999). Are the Pacific and Indo-Atlantic hotspots fixed? Testing the plate circuit through Antarctica. *Earth and Planetary Science Letters*, *170*(1–2), 105–117. https://doi.org/10.1016/S0012-821X(99)00096-5

Domeier, M., Shephard, G. E., Johannes, J., Gaina, C., Doubrovine, P. V., & Torsvik, T. H. (2017). Intraoceanic subduction spanned the Pacific in the Late Cretaceous–Paleocene. *Science Advances*, *3*(11), 1–6. https://doi.org/10.1126/sciadv.aao2303

Domeier, M., & Torsvik, T. H. (2014). *Plate tectonics in the late Paleozoic*, *Geoscience Frontiers*, (Vol. 5, pp. 303–350). Elsevier Ltd. https://doi.org/10.1016/j.gsf.2014.01.002

Doubrovine, P. V., Steinberger, B., & Torsvik, T. H. (2012). Absolute plate motions in a reference frame defined by moving hot spots in the Pacific, Atlantic, and Indian Oceans. *Journal of Geophysical Research*, *117*, B09101. https://doi.org/10.1029/2011JB009072

Evans, D. A. (1998). True polar wander, a supercontinental legacy. *Earth and Planetary Science Letters*, *157*(1–2), 1–8. https://doi.org/10.1016/S0012-821X(98)00031-4

Evans, D. A. D. (2003). True polar wander and supercontinents. *Tectonophysics*, *362*(1–4), 303–320. https://doi.org/10.1016/S0040-1951(02)000642-X

Flament, N., Williams, S., Müller, R. D., Gurnis, M., & Bower, D. J. (2017). Origin and evolution of the deep thermochemical structure beneath Eurasia. *Nature Communications*, *8*(1), 14,164. https://doi.org/10.1038/ncomms14164

Gordon, R. G., & Jurdy, D. M. (1986). Cenozoic global plate motions. *Journal of Geophysical Research*, *91*(B12), 12,389–12,406. https://doi.org/10.1029/JB091ib12p12389

Gordon, R. G., & Stein, S. (1992). Global tectonics and space geodesy. *Science*, *256*(5055), 333–342. https://doi.org/10.1126/science.256.5055.333

Gripp, A. E., & Gordon, R. G. (2002). Young tracks of hotspots and current plate velocities. *Geophysical Journal International*, *150*(2), 321–361. https://doi.org/10.1046/j.1365-246X.2002.01627.x

Gurnis, M., Turner, M., Zahirovic, S., DiCaprio, L., Spasojevic, S., Müller, R. D., et al. (2012). Plate tectonic reconstructions with continuously closing plates. *Computational Geosciences*, *38*(1), 35–42. https://doi.org/10.1016/j.cageo.2011.04.014

Hassan, R., Müller, R. D., Gurnis, M., Williams, S. E., & Flament, N. (2016). A rapid burst in hotspot motion through the interaction of tectonics and deep mantle flow. *Nature*, *533*(7602), 239–242. https://doi.org/10.1038/nature17422

Hellinger, S. (1981). The uncertainties of finite rotations in plate tectonics. *Journal of Geophysical Research*, *86*(B10), 9312–9318. https://doi.org/10.1029/JB086iB10p09312

Herlihy, M., & Shavit, N. (2012). *The art of multiprocessor programming*. Revised Reprint. Elsevier.

Hoernle, K., Rohde, J., Hauff, F., Garbe-Schönberg, D., Homrighausen, S., Werner, R., & Morgan, J. P. (2015). How and when plume zonation appeared during the 132 Myr evolution of the Tristan Hotspot. *Nature Communications*, *6*(1), 7799. https://doi.org/10.1038/ncomms8799

Johnson, S. G. (2016), The NLopt nonlinear-optimization package, Available from: http://ab-initio.mit.edu/nlopt

Jones, D. L., Duncan, R. A., Briden, J. C., Randall, D. E., & MacNiocaill, C. (2001). Age of the Batoka basalts, northern Zimbabwe, and the duration of Karoo Large Igneous Province magmatism. *Geochemistry, Geophysics, Geosystems*, *2*(2). https://doi.org/10.1029/2000GC000110

Kaula, W. M. (1975). Absolute plate motions by boundary velocity minimizations. *Journal of Geophysical Research*, *80*(2), 244–248. https://doi.org/10.1029/JB080i002p00244

Kirschvink, J. L. (1997). Evidence for a large-scale reorganization of Early Cambrian continental masses by inertial interchange True Polar Wander. *Science*, *277*(5325), 541–545. https://doi.org/10.1126/science.277.5325.541

Knesel, K. M., Cohen, B. E., Vasconcelos, P. M., & Thiede, D. S. (2008). Rapid change in drift of the Australian plate records collision with Ontong Java plateau. *Nature*, *454*(7205), 754–757. https://doi.org/10.1038/nature07138

Koivisto, E. A., Andrews, D. L., & Gordon, R. G. (2014). Tests of fixity of the Indo-Atlantic hot spots relative to Pacific hot spots. *Journal of Geophysical Research: Solid Earth*, *119*, 661–675. https://doi.org/10.1002/2013JB010413

Konrad, K., Koppers, A. A. P., Steinberger, B., Finlayson, V. A., Konter, J. G., & Jackson, M. G. (2018). On the relative motions of long-lived Pacific mantle plumes. *Nature Communications*. Springer US, *9*(1), 854. https://doi.org/10.1038/s41467-018-03277-x

Koppers, A. A. P., Gowen, M. D., Colwell, L. E., Gee, J. S., Lonsdale, P. F., Mahoney, J. J., & Duncan, R. A. (2011). New $^{40}Ar/^{39}Ar$ age progression for the Louisville hot spot trail and implications for inter-hot spot motion. *Geochemistry, Geophysics, Geosystems*, *12*, Q0AM02. https://doi.org/10.1029/2011GC003804

Koppers, A. A. P., Steinberger, B., & Duncan, R. A. (2004). Implications of a nonlinear $^{40}Ar/^{39}Ar$ age progression along the Louisville seamount trail for models of fixed and moving hot spots. *Geochemistry, Geophysics, Geosystems*, *5*, Q06L02. https://doi.org/10.1029/2003GC000671

Koppers, A. A. P., Yamazaki, T., Geldmacher, J., Gee, J. S., Pressling, N., Koppers, A. A. P., et al. (2012). Limited latitudinal mantle plume motion for the Louisville hotspot. *Nature Geoscience*, *5*(12), 911–917. https://doi.org/10.1038/NGEO1638

Lallemand, S., Heuret, A., Faccenna, C., & Funiciello, F. (2008). Subduction dynamics as revealed by trench migration. *Tectonics*, *27*, TC3014. https://doi.org/10.1029/2007TC002212

Li, Z. X., Evans, D. A. D., & Zhang, S. (2004). A 90° spin on Rodinia: Possible causal links between the Neoproterozoic supercontinent, superplume, true polar wander and low-latitude glaciation. *Earth and Planetary Science Letters*, *220*(3-4), 409–421. https://doi.org/10.1016/S0012-821X(04)00064-0

Li, Z.-X., & Zhong, S. (2009). Supercontinent–superplume coupling, true polar wander and plume mobility: Plate dominance in whole-mantle tectonics. *Physics of the Earth and Planetary Interiors*, *176*(3–4), 143–156. https://doi.org/10.1016/j.pepi.2009.05.004

Maher, S. M., Wessel, P., Muller, R. D., Williams, S. E., & Harada, Y. (2015). Absolute plate motion of Africa around Hawaii-Emperor bend time. *Geophysical Journal International*, *201*(3), 1743–1764. https://doi.org/10.1093/gji/ggv104

Matthews, K. J., Müller, R. D., Wessel, P., & Whittaker, J. M. (2011). The tectonic fabric of the ocean basins. *Journal of Geophysical Research*, *116*, B12109. https://doi.org/10.1029/2011JB008413

Matthews, K. J., Williams, S. E., Whittaker, J. M., Müller, R. D., Seton, M., & Clarke, G. L. (2015). Geologic and kinematic constraints on Late Cretaceous to mid Eocene plate boundaries in the southwest Pacific. *Earth-Science Reviews*, *140*, 72–107. https://doi.org/10.1016/j.earscirev.2014.10.008

McDougall, I., & Duncan, R. A. (1988). Age progressive volcanism in the Tasmantid Seamounts. *Earth and Planetary Science Letters*, *89*(2), 207–220. https://doi.org/10.1016/0012-821X(88)90173-2

McNamara, A. K., & Zhong, S. (2004). Thermochemical structures within a spherical mantle: Superplumes or piles? *Journal of Geophysical Research*, *109*, B07402. https://doi.org/10.1029/2003JB002847

McNamara, A. K., & Zhong, S. (2005). Thermochemical structures beneath Africa and the Pacific Ocean. *Nature*, *437*(7062), 1136–1139. https://doi.org/10.1038/nature04066

Merdith, A. S., Collins, A. S., Williams, S. E., Pisarevsky, S., Foden, J. D., Archibald, D. B., et al. (2017). A full-plate global reconstruction of the Neoproterozoic. *Gondwana Research*, *50*, 84–134. https://doi.org/10.1016/j.gr.2017.04.001

Mitchell, R. N., Kilian, T. M., & Evans, D. A. D. (2012). Supercontinent cycles and the calculation of absolute palaeolongitude in deep time. *Nature*, *482*(7384), 208–211. https://doi.org/10.1038/nature10800

Molnar, P., & Atwater, T. (1973). Relative motion of hot spots in the mantle. *Nature*, *246*(5431), 288–291. https://doi.org/10.1038/246288a0

Molnar, P., & Stock, J. (1987). Relative motions of hotspots in the Pacific, Atlantic and Indian Oceans since late cretaceous time. *Nature*, *327*(6123), 587–591. https://doi.org/10.1038/327587a0

Morgan, W. J. (1971). Convection plumes in the lower mantle. *Nature*, *230*(5288), 42–43. https://doi.org/10.1038/230042a0

Müller, R. D., Cannon, J., Qin, X., Watson, R. J., Gurnis, M., Williams, S., et al. (2018). GPlates: Building a virtual Earth through deep time. *Geochemistry, Geophysics, Geosystems*. John Wiley & Sons, Ltd, *19*, 2243–2261. https://doi.org/10.1029/2018GC007584

Müller, R. D., Roest, W. R., Royer, J. Y., Gahagan, L. M., & Sclater, J. G. (1997). Digital isochrons of the world's ocean floor. *Journal of Geophysical Research*, *102*(B2), 3211–3214. https://doi.org/10.1029/96JB01781

Muller, R. D., Royer, J. Y., & Lawver, L. A. (1993). Revised plate motions relative to the hotspots from combined Atlantic and Indian Ocean hotspot tracks. *Geology*, *21*(3), 275–278. https://doi.org/10.1130/0091-7613(1993)021<0275:RPMRTT>2.3.CO;2

Müller, R. D., Seton, M., Zahirovic, S., Williams, S. E., Matthews, K. J., Wright, N. M., et al. (2016). Ocean basin evolution and global-scale reorganization events since Pangea breakup. *Annual Review of Earth and Planetary Sciences*, *44*(1), 107–138. https://doi.org/10.1146/annurev-earth-060115-012211

Müller, R. D., Zahirovic, S., Williams, S. E., Cannon, J., Seton, M., Bower, D. J., & Gurnis, M. (2019). A global plate model including lithospheric deformation along major rifts and orogens since the Triassic. *Tectonics*, *38*. https://doi.org/10.1029/2018TC005462

O'Connor, J. M., Steinberger, B., Regelous, M., Koppers, A. A. P., Wijbrans, J. R., Haase, K. M., et al. (2013). Constraints on past plate and mantle motion from new ages for the Hawaiian-Emperor Seamount Chain. *Geochemistry, Geophysics, Geosystems*, *14*, 4564–4584. https://doi.org/10.1002/ggge.20267

O'Neill, C. (2005). Insulation and depletion due to thickened crust: Effects on melt production on Mars and Earth. *Geophysical Research Letters*, *32*, L14304. https://doi.org/10.1029/2005GL022855

O'Neill, C., Müller, D., & Steinberger, B. (2003). Geodynamic implications of moving Indian Ocean hotspots. *Earth and Planetary Science Letters*, *215*(1–2), 151–168. https://doi.org/10.1016/S0012-821X(03)00368-6

O'Neill, C., Müller, D., & Steinberger, B. (2005). On the uncertainties in hot spot reconstructions and the significance of moving hot spot reference frames. *Geochemistry, Geophysics, Geosystems*, *6*, Q04003. https://doi.org/10.1029/2004GC000784

Powell, M. J. D. (1994). A direct search optimization method that models the objective and constraint functions by linear interpolation. In *Advances in optimization and numerical analysis*, (pp. 51–67). Dordrecht: Springer Netherlands. https://doi.org/10.1007/978-94-015-8330-5_4

Powell, M. J. D. (1998). Direct search algorithms for optimization calculations. *Acta Numerica*, *7*, 287. https://doi.org/10.1017/S0962492900002841

Powell, M. J. D. (2007). A view of algorithms for optimization without derivatives. *Mathematics Today-Bulletin of the Institute of Mathematics and Its Applications*, *43*(5), 1–12.

Schellart, W. P., Lister, G. S., & Toy, V. G. (2006). A Late Cretaceous and Cenozoic reconstruction of the Southwest Pacific region: Tectonics controlled by subduction and slab rollback processes. *Earth-Science Reviews*, *76*(3–4), 191–233. https://doi.org/10.1016/j.earscirev.2006.01.002

Schellart, W. P., Stegman, D. R., & Freeman, J. (2008). Global trench migration velocities and slab migration induced upper mantle volume fluxes: Constraints to find an Earth reference frame based on minimizing viscous dissipation. *Earth-Science Reviews*, *88*(1–2), 118–144. https://doi.org/10.1016/j.earscirev.2008.01.005

Schettino, A., & Scotese, C. R. (2005). Apparent polar wander paths for the major continents (200 Ma to the present day): A palaeomagnetic reference frame for global plate tectonic reconstructions. *Geophysical Journal International*, *163*(2), 727–759. https://doi.org/10.1111/j.1365-246X.2005.02638.x

Schneider, D. A., & Kent, D. V. (1990). Paleomagnetism of Leg 115 sediments: Implications for Neogene magnetostratigraphy and paleolatitude of the Réunion Hotspot. *Proceedings of the Ocean Drilling Program, Scientific Results*, *115*, 717–736.

Seton, M., Müller, R. D., Zahirovic, S., Gaina, C., Torsvik, T., Shephard, G., et al. (2012). Global continental and ocean basin reconstructions since 200 Ma. *Earth-Science Reviews*, *113*(3-4), 212–270. https://doi.org/10.1016/j.earscirev.2012.03.002

Shephard, G. E., Bunge, H. P., Schuberth, B. S. A., Müller, R. D., Talsma, A. S., Moder, C., & Landgrebe, T. C. W. (2012). Testing absolute plate reference frames and the implications for the generation of geodynamic mantle heterogeneity structure. *Earth and Planetary Science Letters*, *317-318*, 204–217. https://doi.org/10.1016/j.epsl.2011.11.027

Shephard, G. E., Müller, R. D., & Seton, M. (2013). The tectonic evolution of the Arctic since Pangea breakup: Integrating constraints from surface geology and geophysics with mantle structure. *Earth-Science Reviews*, *124*, 148–183. https://doi.org/10.1016/j.earscirev.2013.05.012

Steinberger, B. (2000). Plumes in a convecting mantle: Models and observations for individual hotspots. *Journal of Geophysical Research*, *105*(B5), 11127–11152. https://doi.org/10.1029/1999JB900398

Steinberger, B., & O'Connell, R. J. (1998). Advection of plumes in mantle flow: Implications for hotspot motion, mantle viscosity and plume distribution. *Geophysical Journal International*, *132*(2), 412–434. https://doi.org/10.1046/j.1365-246x.1998.00447.x

Steinberger, B., Sutherland, R., & O'Connell, R. J. (2004). Prediction of Emperor-Hawaii seamount locations from a revised model of global plate motion and mantle flow. *Nature*, *430*(6996), 167–173. https://doi.org/10.1038/nature02660

Steinberger, B., & Torsvik, T. H. (2008). Absolute plate motions and true polar wander in the absence of hotspot tracks. *Nature*, *452*(7187), 620–623. https://doi.org/10.1038/nature06824

Stock, J., & Molnar, P. (1982). Uncertainties in the relative positions of the Australia, Antarctica, Lord Howe, and Pacific Plates since the Late Cretaceous. *Journal of Geophysical Research*, *87*(B6), 4697–4714. https://doi.org/10.1029/JB087iB06p04697

Tan, E., & Gurnis, M. (2005). Metastable superplumes and mantle compressibility. *Geophysical Research Letters*, *32*, L20307. https://doi.org/10.1029/2005GL024190

Tan, E., & Gurnis, M. (2007). Compressible thermochemical convection and application to lower mantle structures. *Journal of Geophysical Research*, *112*, B06304. https://doi.org/10.1029/2006JB004505

Tarduno, J., Bunge, H.-P., Sleep, N., & Hansen, U. (2009). The bent Hawaiian-Emperor hotspot track: Inheriting the mantle wind. *Science*, *324*(5923), 50–53. https://doi.org/10.1126/science.1161256

Tarduno, J. A., Duncan, R. A., Scholl, D. W., Cottrell, R. D., Steinberger, B., Thordarson, T., et al. (2003). The Emperor Seamounts: Southward motion of the Hawaiian hotspot plume in Earth's mantle. *Science*, *301*(5636), 1064–1069. https://doi.org/10.1126/science.1086442

Tauxe, L. (2010). *Essentials of paleomagnetism*. University of California Press.

Tetley, M. G., Li, Z.-X., Matthews, K. J., Williams, S. E., & Müller, R. D. (2019). Decoding earth's plate tectonic history using sparse geochemical data. *Geoscience Frontiers*. https://doi.org/10.1016/j.gsf.2019.05.002

Torsvik, T. H. (2018). Earth history: A journey in time and space from base to top. *Tectonophysics*, *760*, 297–313. https://doi.org/10.1016/j.tecto.2018.09.009

Torsvik, T. H., & Cocks, L. R. M. (2016). *Earth history and palaeogeography*. Cambridge: Cambridge University Press. https://doi.org/10.1017/9781316225523

Torsvik, T. H., Doubrovine, P. V., Steinberger, B., Gaina, C., Spakman, W., & Domeier, M. (2017). Pacific plate motion change caused the Hawaiian-Emperor Bend. *Nature Communications*, *8*(1). https://doi.org/10.1038/ncomms15660

Torsvik, T. H., Müller, R. D., Van der Voo, R., Steinberger, B., & Gaina, C. (2008). Global plate motion frames: Toward a unified model. *Reviews of Geophysics*, *46*, RG3004. https://doi.org/10.1029/2007RG000227

Torsvik, T. H., Smethurst, M. A., Burke, K., & Steinberger, B. (2006). Large igneous provinces generated from the margins of the large low-velocity provinces in the deep mantle. *Geophysical Journal International*, *167*(3), 1447–1460. https://doi.org/10.1111/j.1365-246X.2006.03158.x

Torsvik, T. H., Steinberger, B., Cocks, L. R. M., & Burke, K. (2008). Longitude: Linking Earth's ancient surface to its deep interior. *Earth and Planetary Science Letters*, *276*(3–4), 273–282. https://doi.org/10.1016/j.epsl.2008.09.026

Torsvik, T. H., Steinberger, B., Gurnis, M., & Gaina, C. (2010). Plate tectonics and net lithosphere rotation over the past 150 My. *Earth and Planetary Science Letters*, *291*(1–4), 106–112. https://doi.org/10.1016/j.epsl.2009.12.055

Torsvik, T. H., van der Voo, R., Preeden, U., Mac Niocaill, C., Steinberger, B., Doubrovine, P. V., et al. (2012). Phanerozoic polar wander, palaeogeography and dynamics. *Earth-Science Reviews*, *114*(3–4), 325–368. https://doi.org/10.1016/j.earscirev.2012.06.007

Tsai, V. C., & Stevenson, D. J. (2007). Theoretical constraints on true polar wander. *Journal of Geophysical Research*, *112*, B05415. https://doi.org/10.1029/2005JB003923

Vandamme, D., & Courtillot, V. (1990). Latitudinal evolution of the Réunion hotspot deduced from paleomagnetic results of Leg 115. *Geophysical Research Letters*, *17*(8), 1105–1108. https://doi.org/10.1029/GL017i008p01105

Van der Voo, R. (1990). The reliability of paleomagnetic data. *Tectonophysics*, *184*(1), 1–9. https://doi.org/10.1016/0040-1951(90)90116-P

van der Meer, D. G., Spakman, W., van Hinsbergen, D. J. J., Amaru, M. L., & Torsvik, T. H. (2010). Towards absolute plate motions constrained by lower-mantle slab remnants. *Nature Geoscience*, *3*(1), 36–40. https://doi.org/10.1038/ngeo708

van der Meer, D. G., Torsvik, T. H., Spakman, W., Van Hinsbergen, D. J. J., & Amaru, M. L. (2012). Intra-Panthalassa Ocean subduction zones revealed by fossil arcs and mantle structure. *Nature Geoscience*, *5*(3), 215–219. https://doi.org/10.1038/ngeo1401

van der Meer, D. G., van Hinsbergen, D. J. J., & Spakman, W. (2018). Atlas of the underworld: Slab remnants in the mantle, their sinking history, and a new outlook on lower mantle viscosity. *Tectonophysics*, *723*, 309–448. https://doi.org/10.1016/j.tecto.2017.10.004

Wang, C., Gordon, R. G., & Zhang, T. (2017). Bounds on geologically current rates of motion of groups of hot spots. *Geophysical Research Letters*, *44*, 6048–6056. https://doi.org/10.1002/2017GL073430

Wang, H., Wang, Y., Gurnis, M., Zahirovic, S., & Leng, W. (2018). A long-lived Indian Ocean slab: Deep dip reversal induced by the African LLSVP. *Earth and Planetary Science Letters*, *497*, 1–11. https://doi.org/10.1016/j.epsl.2018.05.050

Wessel, P., & Kroenke, L. W. (1998). The geometric relationship between hot spots and seamounts: Implications for Pacific hot spots. *Earth and Planetary Science Letters*, *158*(1–2), 1–18. https://doi.org/10.1016/S0012-821X(98)00043-0

Wessel, P., & Kroenke, L. W. (2008). Pacific absolute plate motion since 145 Ma: An assessment of the fixed hot spot hypothesis. *Journal of Geophysical Research*, *113*, B06101. https://doi.org/10.1029/2007JB005499

Wessel, P., & Müller, R. D. (2016). Ridge-spotting: A new test for Pacific absolute plate motion models. *Geochemistry, Geophysics, Geosystems*, *17*, 2408–2420. https://doi.org/10.1002/2016GC006404

Williams, S., Flament, N., & Müller, R. D. (2016). Alignment between seafloor spreading directions and absolute plate motions through time. *Geophysical Research Letters*, *43*, 1472–1480. https://doi.org/10.1002/2015GL067155

Williams, S., Flament, N., Müller, R. D., & Butterworth, N. (2015). Absolute plate motions since 130 Ma constrained by subduction zone kinematics. *Earth and Planetary Science Letters*, *418*, 66–77. https://doi.org/10.1016/j.epsl.2015.02.026

Wilson, J. T. (1963). Evidence from islands on the spreading of ocean floors. *Nature*, *197*(4867), 536–538. https://doi.org/10.1038/197536a0

Zahirovic, S., Müller, R. D., Seton, M., & Flament, N. (2015). Tectonic speed limits from plate kinematic reconstructions. *Earth and Planetary Science Letters*, *418*, 40–52. https://doi.org/10.1016/j.epsl.2015.02.037

Zahirovic, S., Müller, R. D., Seton, M., Flament, N., Gurnis, M., & Whittaker, J. (2012). Insights on the kinematics of the India-Eurasia collision from global geodynamic models. *Geochemistry, Geophysics, Geosystems*, *13*, Q04W11. https://doi.org/10.1029/2011GC003883

Zhong, S. J. (2001). Role of ocean-continent contrast and continental keels on plate motion, net rotation of lithosphere, and the geoid. *Journal of Geophysical Research*, *106*(B1), 703–712. https://doi.org/10.1029/2000JB900364